On the implementation of perfectly matched layers in a three-dimensional fourth-order velocity-stress finite difference scheme

Carey Marcinkovich[1] and Kim Olsen

Institute for Crustal Studies, University of California, Santa Barbara, California, USA

[1] Robust absorbing boundary conditions are central to the utility and advancement of 3-D numerical wave propagation methods. It is in general preferred that an absorbing boundary method be capable of broadband absorption, be efficient in terms of memory and computation time, and be widely stable in connection with sophisticated numerical schemes. Here we discuss these issues for a promising absorbing boundary method, perfectly matched layers (PML), as implemented in the widely used fourth-order accurate three-dimensional (3-D) staggered-grid velocity-stress finite difference (FD) scheme. Numerical results for point (explosive and double couple) and extended sources, velocity structures (homogeneous, 1-D and 3-D), and different thickness PML zones are excellent, in general, leaving no observable reflections in PML seismograms compared to the amplitudes of the primary phases. For both homogeneous half-space and 1-D models, typical amplitude reduction factors (with respect to the maximum trace amplitude) range between 1/100 and 1/625 for PML thicknesses of 5–20 nodes. A PML region of thickness 5 outperforms a simple exponential damping region of thickness 20 in a homogeneous half-space model by a factor of 3. We find that PML is effective across the simulation bandwidth. For example, permanent offset artifacts due to particularly poor absorption of long-period energy by the simple exponential damping are effectively absent when PML is used. The computational efficiency and storage requirements of PML, compared to the simple exponential damping, are reduced due to the need for only narrow absorbing regions. We also discuss stability and present the complete PML model for the 3-D velocity-stress system.   *INDEX TERMS:* 0902 Exploration Geophysics: Computational methods, seismic; 3230 Mathematical Geophysics: Numerical solutions; 7212 Seismology: Earthquake ground motions and engineering; 7260 Seismology: Theory and modeling; 7299 Seismology: General or miscellaneous; *KEYWORDS:* finite differences, numerical modeling, absorbing boundary conditions, three-dimensional simulations, wave propagation, perfectly matched layers

Citation: Marcinkovich, C., and K. Olsen, On the implementation of perfectly matched layers in a three-dimensional fourth-order velocity-stress finite difference scheme, *J. Geophys. Res.*, *108*(B5), 2276, doi:10.1029/2002JB002235, 2003.

1. Introduction

[2] A large variety of absorbing boundary conditions used in elastodynamics have been presented in the literature. While most of these conditions are used along the outermost boundary of the grid [e.g., *Clayton and Engquist*, 1977; *Higdon*, 1986, 1990; *Reynolds*, 1978; *Randall*, 1988, and many others], an important class of absorbers are applied within regions of finite thickness. A relatively new member of the latter group is PML (perfectly matched layers). Presented in 2-D [*Berenger*, 1994] and 3-D [*Berenger*, 1996] time domain EM simulations, PML has since been used extensively in that field. PML has also been incorporated into a variety of wave propagation algorithms, but its infusion into elastodynamics has been comparatively slow. PML was first formulated for the P-SV case in an approach that utilized potentials in the PML region [*Hastings et al.*, 1996]. Excellent results were achieved in this 2-D finite difference scheme; however, its applicability was limited to models without heterogeneity in the PML regions. *Chew and Liu* [1996] formulated and demonstrated PML for 2-D and 3-D elastodynamics using a leapfrog scheme in homogeneous and heterogeneous media, including fluid-solid interfaces. More recently, a technique for acoustics in absorptive media was developed for 2-D and 3-D simulations [*Liu and Tao*, 1997]. It was shown that in the presence of intrinsic attenuation, an additional time-integrated pressure field term is required to account for the coupling of loss between the PML and intrinsic absorptions. PML has also been applied to the poroelastic wave equations in 2-D media

[1]Now at ExxonMobil Exploration Company, 222 Benmar, Houston, Texas, USA.

[*Zeng and Liu*, 2001; *Zeng et al.*, 2001]. *Collino and Tsogka* [2001] have formulated and demonstrated PML in the P-SV case via the *Virieux* [1986] finite difference scheme and a mixed finite element algorithm. Excellent results were demonstrated in homogeneous and heterogeneous media, including anisotropy in the finite element scheme.

[3] While the previous finite difference studies have thoroughly tested PML in unbounded media, the difference operators were of lower order and a free surface was not included, which precludes the analysis of PML's performance in the presence of surface waves. Therefore we further examine the efficacy of the PML technique in the case of a widely used algorithm: a 3-D, staggered-grid, velocity-stress finite difference scheme. We will conduct our analysis for the 2−4 implementation (second-order accurate in time and fourth-order accurate in space), which has become increasingly popular for simulating ground motion, both for kinematic [e.g., *Olsen*, 1994; *Olsen et al.*, 1995; *Olsen and Archuleta*, 1996; *Graves*, 1998; *Wald and Graves*, 1998; *Olsen*, 2000; *Olsen et al.*, 2000; *Olsen*, 2001] and dynamic [e.g., *Olsen et al.*, 1997; *Nielsen and Olsen*, 2000; *Peyrat et al.*, 2001] methods. Additionally, we examine PML's applicability to 3-D heterogeneous media.

[4] We have organized our study of PML as follows. In the next section, the PML formulation and discretization for the 3-D staggered-grid scheme are explained. The following section provides results for a number of numerical examples, including PML implementations in homogeneous, 1-D and 3-D media, for point (explosive and double-couple) and extended sources, and comparisons of the performance and efficiency with the popular *Cerjan et al.* [1985] scheme. In the appendices, we review the 3-D velocity-stress formulation (section A1) and present continuous and discretized versions of the 3-D PML model (sections A2 and A3).

2. PML Implementation

2.1. Formulation

[5] The PML model can be formulated through a simple time domain, equation-splitting procedure. That is, in the elastic case, each wave field equation is split into perpendicular and parallel components, with a damping term being added to the perpendicular term [*Hastings et al.*, 1996; *Collino and Tsogka*, 2001]. It has been shown that such a system of split and damped elastodynamic equations possess two fundamental properties. The first is that the interface between the internal propagation space and the PML space, in a continuum, is nonreflective, which holds even in the case of coupled compressional and shear energy [*Chew and Liu*, 1996]. The second property is that exponential attenuation is present in the nonphysical PML region [*Chew and Liu*, 1996; *Collino and Tsogka*, 2001]. The equation-splitting procedure can also be understood from a complex coordinate stretching (change of complex variable) approach [*Chew and Liu*, 1996; *Collino and Tsogka*, 2001]. That is, in the case of a complex-plane variable change that includes an imaginary term, a split equation results in the time domain. Hereafter, the internal propagation space (model space less the PML absorbing regions) is referred to as the interior region or just the interior, and the PML region/interior region junction is referred to as the
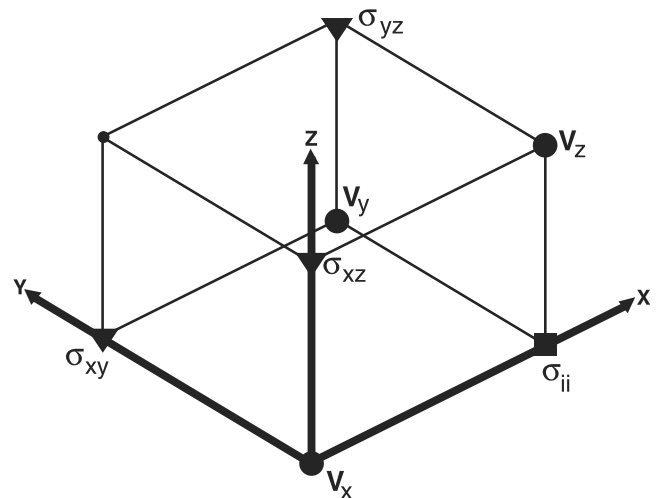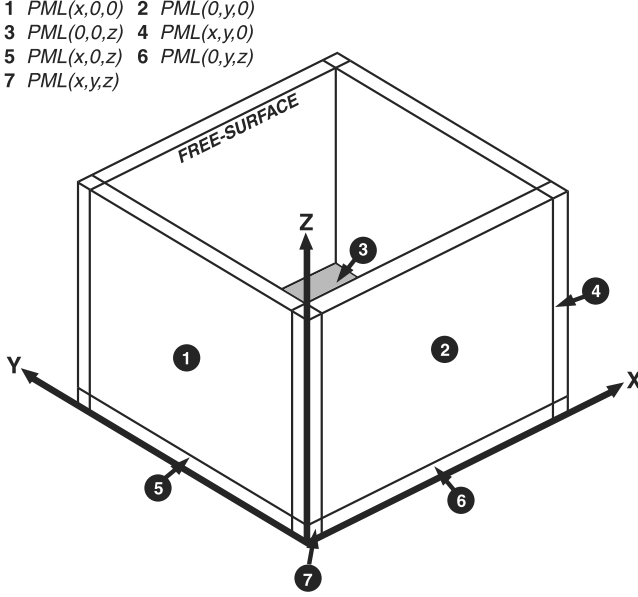

Figure 1. Staggered-grid material cell; V_x is located at the coordinate system origin, and the free surface is located on the V_z plane. Coordinate directions correspond to geographic directions X (east), Y (north) and Z (up).

PML interface. Also, PML region thicknesses are specified in nodes.

[6] Starting with the Cartesian-grid velocity-stress system (section A1), each equation is split into a parallel and perpendicular component, based on spatial derivative separation. That is, the perpendicular equation contains the spatial derivative term which acts normal to the coordinate plane of interest and a damping term, and the parallel equation contains the remaining spatial derivative terms. Finally, an additional equation is required to sum the results of the split equations. For the 3-D velocity-stress system, a PML model can be formulated for each of the three coordinate directions, providing damping for the bounding side and bottom regions in a 3-D model space; such an approach results in 81 equations. In particular, for an X plane, the perpendicular equations contain the appropriate perpendicular velocity or stress term, a damping term and the spatial derivative term (when present) acting in the X direction. The parallel equations contain the appropriate parallel velocity or stress term and the spatial derivative terms (when present) that act in the Y and Z directions (section A2). Similar systems can be formulated for the Y and Z planes (section A2). The horizontal edges, vertical edges and corners require multiple damping terms, which we reserve for the following discussion on discretization.

2.2. Discretization

[7] Before discussing the PML discretization, we note a few relevant characteristics of the FD scheme with which the PML formulation is solved. The scheme solves the 3-D elastic wave equation in the velocity-stress formulation [*Madariaga*, 1976; *Virieux and Madariaga*, 1982; *Virieux*, 1986] which we describe in section A1. Our particular development is for a fourth-order velocity-stress scheme [*Olsen*, 1994] and is solved on a regular staggered grid. It includes a second-order planar free surface, which places the vertical velocity component (V_z) and the xz (σ_{xz}) and yz (σ_{yz}) components of the stress directly on the free surface FS2 of *Gottschämmer and Olsen* [2001] (see Figure 1). We

1 *PML(x,0,0)* 2 *PML(0,y,0)*
3 *PML(0,0,z)* 4 *PML(x,y,0)*
5 *PML(x,0,z)* 6 *PML(0,y,z)*
7 *PML(x,y,z)*

Figure 2. Propagation space for FD simulations with the PML models at the boundary regions; conventional propagation is carried out in model space interior. In numbered boundary zones (and complementary zones) the PML model is invoked. Plane regions require damping in their normal direction, e.g., PML(x, 0, 0) for plane 1. Vertical and horizontal edges are damped in both directions of their bounding planes, e.g., PML(x, y, 0) for vertical edge 4. Corners are damped in all three coordinate directions, e.g., PML(x, y, z) for corner 7.

take the following coordinate directions as positive, as shown in the FD material cell (Figure 1): east (X), north (Y) and up (Z).

[8] The PML formulation described above (see also section A2) can be discretized and solved using the conventional staggered-grid finite difference technique. However, such an approach does not directly suggest a damping technique for the corners and edges, nor does PML theory present an obvious approach. Thus, following *Collino and Tsogka* [2001], we present a compact, discretized version of the 3-D velocity-stress PML equations that provides for absorption in all 17 PML regions (Figure 2). To form the discretized version, each variable of the propagation system is split into three separate perpendicular equations; that is, each coordinate direction is taken as the perpendicular. This results in three equations for each wave field variable (four counting the summation equation), each with a damping term (section A3). If all three damping terms are nonzero, then the system is appropriate for damping in corner regions. If one damping term is equal to zero, then damping in edge regions is defined. And if only one nonzero damping term exists, plane region damping is implied. In other words, in each PML region, a damping term is applied in the normal direction of each bounding plane. Thus the compact, discretized system implies a method for applying the damping terms in all model space regions. The system is solved directly in the corner and edge regions with appropriate damping values for each region. In the plane regions, two equations result with zero damping; for memory con-

servation, these equations are combined into one parallel equation as presented in the continuum case (section A2).

[9] Our implementation includes a planar free surface, which is considered in the vertical edge and the vertical plane PML regions (X and Y planes). Since the PML regions are solved using second-order operators, only the anti-symmetry condition need be considered for the V_z component; that is, we only need to mirror the σ_{zz} component above the free surface. The stress variables σ_{xz} and σ_{yz} located at the free surface are defined as zero (see Figure 1). Thus the solution of the combined PML and interior systems, in the presence of a free surface, progresses as follows: (1) update interior velocities and perpendicular and parallel PML velocities, (2) sum perpendicular and parallel PML velocities, (3) apply velocity free-surface conditions to interior region, (4) update interior stresses and perpendicular and parallel PML stresses, (5) sum perpendicular and parallel PML stresses, (6) apply anti-symmetry to the σ_{zz} component in PML region, (7) apply stress free-surface conditions to interior region, and (8) repeat.

[10] The final discretization topics to address are the maximum damping parameter selection and the distribution of damping values within the PML region. Upon discretization of the PML system, the reflection-free PML interface no longer exists and is supplanted with PML discretization error that is proportional to the product of the spatial discretization and the damping contrast [*Chew and Liu*, 1996]. *Hastings et al.* [1996] and *Collino and Tsogka* [2001] presented a relation based upon a theoretical reflection coefficient, the PML region thickness and a typical medium velocity. *Zeng and Liu* [2001] and *Zeng et al.* [2001] devised a relation that relies on the dominant source frequency and the PML thickness. We have found that the basic relation presented by *Collino and Tsogka* [2001] serves as a satisfactory guide to compute the maximum damping value in our 3-D velocity-stress scheme. However, we prefer a slightly modified version of their original relation, the primary difference being that we use V_s (prominent velocity in earthquake simulations) rather than V_P dependency

$$d_o = log\left(\frac{1}{R}\right)\frac{\tau V_s}{n_b \Delta h}, \tag{1}$$

where R is the theoretical reflection coefficient, V_s is the representative shear velocity, n_b is the PML thickness in nodes and the tuning parameter τ in practice ranges from about 3 to 4 (see Table 1). It is difficult to recommend a 'best value' of τ in the general case due to absorption efficiency apparently dependent on wave type as well as on the structural variation for heterogeneous models. The

Table 1. Simulation Parameters

	H1	H2	H3	H4	H5
Interior number of E-W grid points	199	49	99	465	453
Interior number of N-S grid points	199	49	99	160	238
Interior number of vertical grid points	100	50	50	60	100
Spatial discretization (m)	225	225	225	400	1000
Temporal discretization (s)	0.0175	0.0175	0.0175	0.020	0.055
Highest frequency modeled (Hz)	2	2	0.75	1.0	0.2
PML tuning parameter (τ)	3.2	4.0	3.1	3.7	3.7

Table 2. Velocity Structures

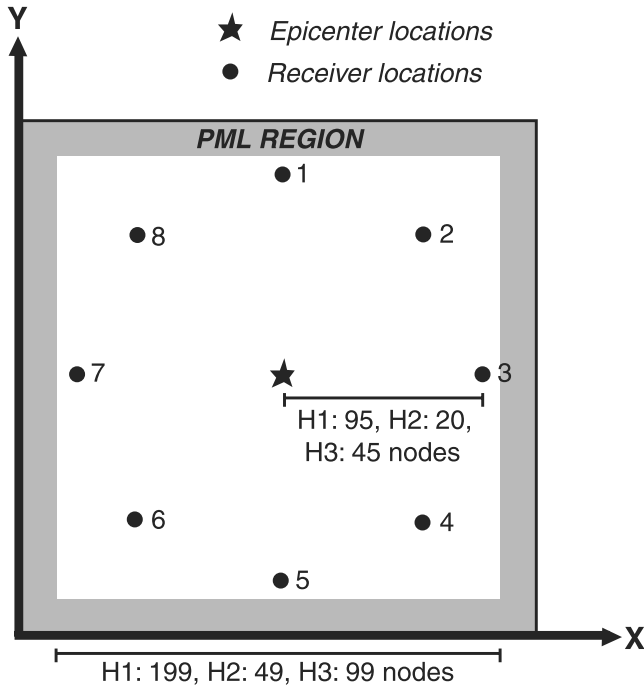|	Structure
M1	homogeneous: V_p 5800 (m/s), V_s 3200 (m/s), ρ 2600 (kg/m^3)
M2	1-D: Los Angeles basin crustal profile, V_s clamped to 1200 (m/s)
M3	1-D: SCEC background crustal profile
M4	3-D: SCEC 3-D velocity structure, V_s clamped to 1400 (m/s)

Table 3. Source Parameters

	Strike, deg	Dip, deg	Rake, deg	Depth, m
S1	130	53	111	1912.5
S2	67	85	10	1912.5
S3	270	31	98	10500.0
S4		Explosive		1912.5

theoretical reflection coefficients are matched with discrete layer thicknesses as follows [*Collino and Tsogka*, 2001]: PML(thickness 5) R = 0.01, PML(10) R = 0.001, and PML(20) R = 0.0001. In order to easily make use of other arbitrary PML thicknesses, we express the relation between the reflection coefficients and the discrete PML widths as a third-order polynomial. Thus the maximum damping value for a PML width between 1 and 20 can be given by

$$d_o = \frac{\tau V_s}{\Delta h}\left(c_1 + c_2 n_b + c_3 n_b^2\right), \tag{2}$$

where n_b is the PML thickness (in nodes), Δh is the grid-spacing, and the polynomial coefficients are $c_1 = \frac{8}{15}$, $c_2 = \frac{-3}{100}$ and $c_3 = \frac{1}{1500}$. The selection of the damping parameter distribution varies among authors [e.g., *Hastings et al.*, 1996; *Chew and Liu*, 1996; *Liu and Tao*, 1997; *Zeng and Liu*, 2001; *Zeng et al.*, 2001; *Collino and Tsogka*, 2001], but is typically of the form

$$d_i = d_o\left(\frac{i}{n_b}\right)^p, \tag{3}$$

where i is the node of interest as counted from the PML interface, and p typically ranges from 1 to 4, with the most commonly presented value giving a quadratic distribution ($p = 2$). We found this value to give the best result in most cases.

3. PML Numerical Results
3.1. Test Parameters

[11] To test the performance and efficiency of the PML implementation, we have constructed five different simulation spaces. The first two (H1 and H2, Table 1) are designed around a half-space (M1, Table 2) and differ only in dimension. H1 accommodates approximately 28 wavelengths of propagation, in the horizontal directions, for the highest frequency in the simulation. The smaller simulation space

Figure 3. Plan view of the propagation space, including variable thickness PML regions. Source location is at the center of the model space with surface-located symmetric array distributed near the PML zones.
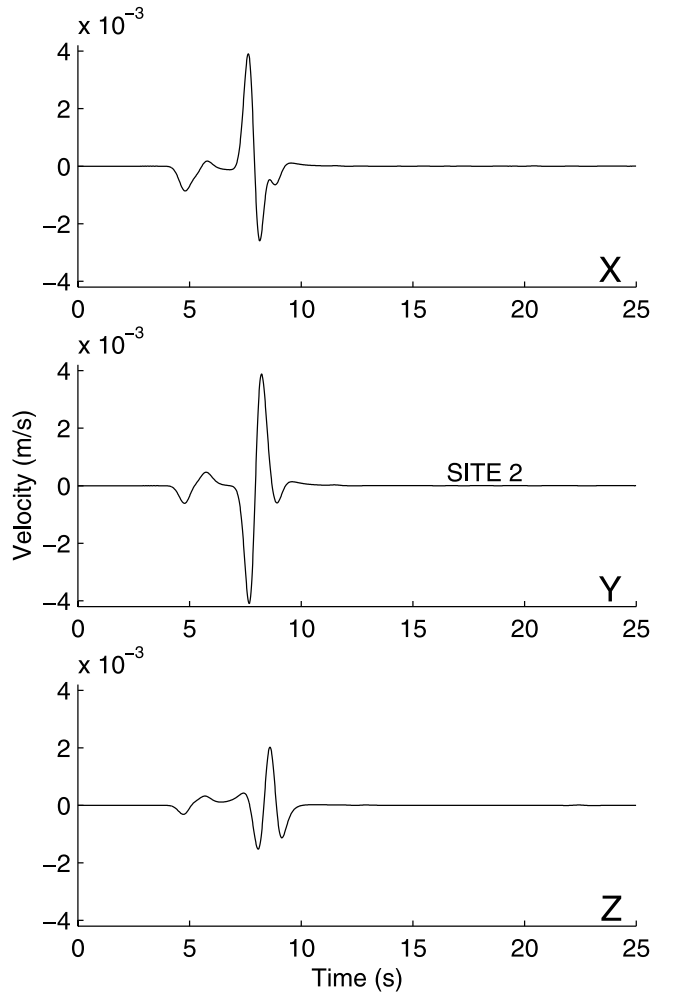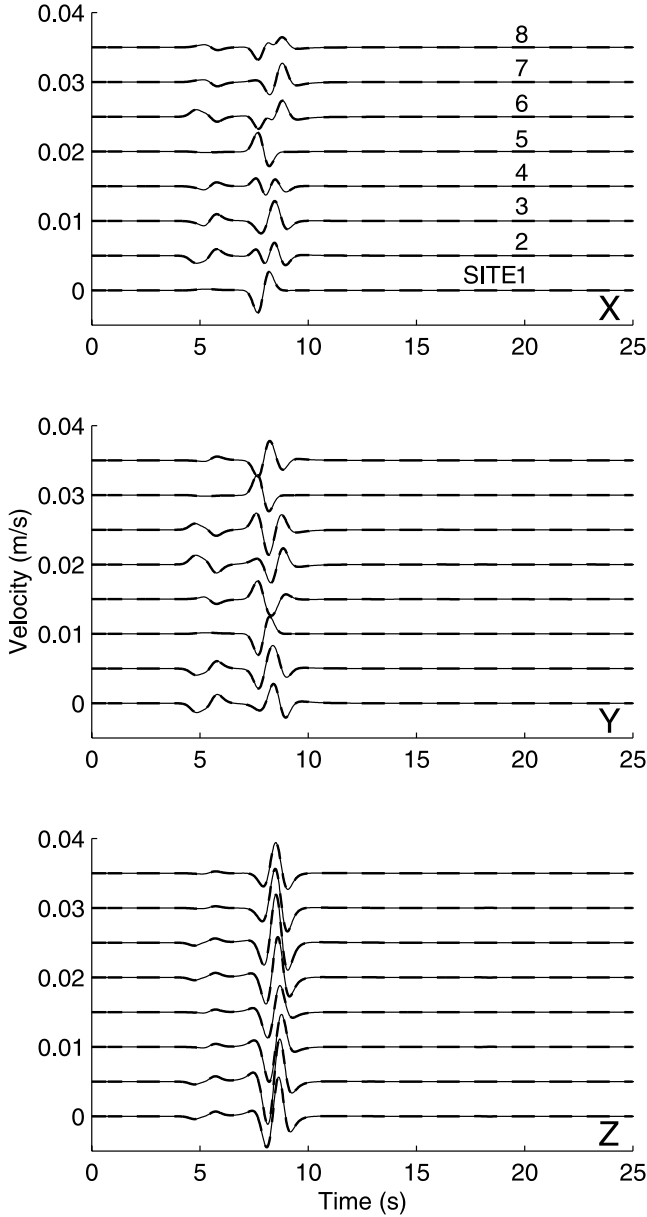

Figure 4. PML simulation recorded at array location 2 (see Figure 3) using space H1, structure M1 and source S2; PML region is 10 nodes in thickness. No observable artificial reflections are observed at the viewing scale.
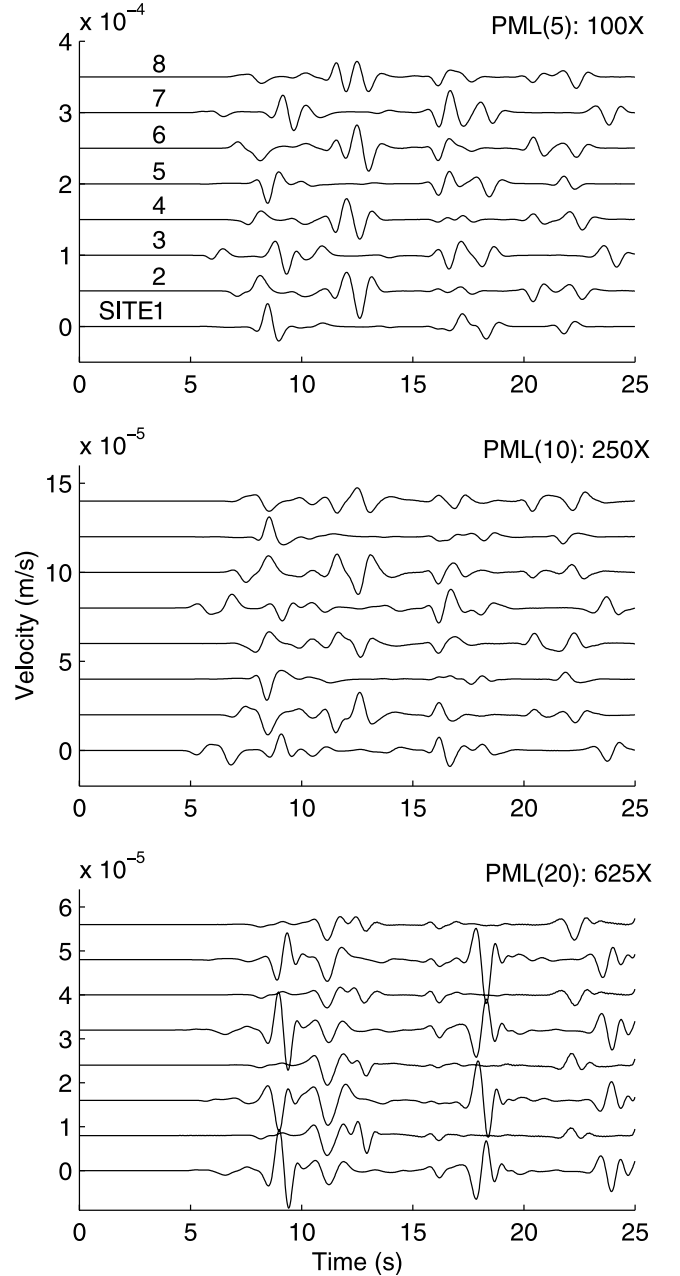
Figure 5. PML simulation (source S1, structure M1, model H1, thick dash) recorded at array locations 1 to 8 (see Figure 3) with respect to reflection-free reference traces (thin solid); PML region is 10 nodes in thickness. No artificial reflections are observed within the array.

detailed description of the source implementation and the resulting ground motion is given by *Olsen* [2001]. Finally, we tested our PML implementation in a fully 3-D heterogeneous model space (H5), covering most of southern California and based on a subset of the SCEC 3-D Reference Structure Version 2.2 (M4). Its primary features are the Los Angeles and San Fernando basins, and the Salton Trough; a portion of the Ventura basin is present in the north-west corner of the simulation space. The model also includes a tomography-based background structure and a variable-depth Moho. For numerical dispersion

(H2) allows for approximately 7 wavelengths of propagation. The third simulation space (H3) is based on a 1-D profile (M2) through the Los Angeles basin and was extracted from the Southern California Earthquake Center (SCEC) 3-D Reference Structure Version 2.2 [*Magistrale et al.*, 2000]. The minimum shear velocity is clamped to 1200 m/s, and the maximum compressional velocity is 6185 m/s. A plan view of the above simulation spaces, along with our 8-station recording array, is shown in Figure 3. We also designed a model space (H4) to simulate an extended rupture on a 170 km long by 15 km deep San Andreas **M** 7.5 fault segment rupture in a 1-D rock profile (M3) where the shear velocities range from 2713 m/s to 4560 m/s. A

Figure 6. Errors for source S1 recorded at array locations 1−8 (see Figure 3) for model H1 and structure M1. PML zones are of width 5 (X), 10 (Y) and 20 (Z). Errors are with respect to reference traces, and are magnified 100, 250 and 625 times for the 5, 10, and 20 width PML regions, respectively.
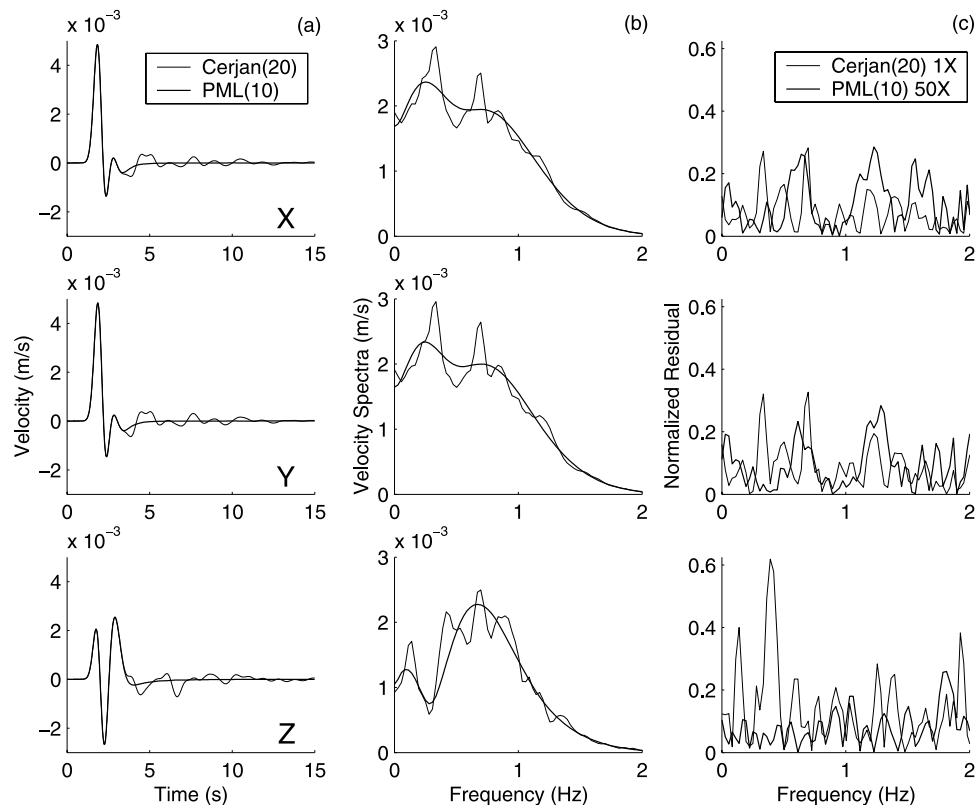
Figure 7. Comparison between PML and Cerjan et al. synthetics recorded at array location 2 (see Figure 3). PML regions are 10 nodes wide (thick solid) and Cerjan et al. regions are 20 nodes in thickness (thin solid) with a damping parameter of 0.92. Source is S4 and structure is M1, in space H2. (a) Particle velocities, (b) amplitude spectra, and (c) normalized residuals. The normalized residuals for PML (magnified 50 times relative to Cerjan et al.) indicate consistent absorption across the spectrum, whereas Cerjan et al. seems to provide its best absorption at higher frequencies.

considerations, the S wave velocities have been clamped to 1400 m/s, and the maximum P wave velocity in the model space is 7800 m/s. This particular simulation space accommodates about 64 wavelengths of propagation along the longest axis. Other relevant modeling parameters are listed in Tables 1 and 2.

[12] We carried out a number of tests in the simulation spaces described above. Several realistic point-source mechanisms were modeled (Table 3), including those after estimates for the 1994 Northridge (S1), the 1999 Hector Mines (S2) and the 1987 Whittier (S3) main shocks, in H1–H3 and H5. The H4 and H5 simulation spaces test, notably, PML's ability to absorb over a wider range of velocities for a complex wave field as well as PML's performance in the presence of heterogeneity in the PML regions themselves. The tests for simulation spaces H1–H3 and H5 are initiated with a Gaussian source time function that provides for small spectral amplitudes at the maximum frequency; typically less than 1/100 of the maximum spectral amplitude. The extended source simulation uses six isosceles triangular source time functions from the kinematic inversion results for the 1992 **M** 7.3 Landers earthquake by *Wald and Heaton* [1994]. We propagate the rupture from the hypocenter (10 km depth) with a rupture velocity of 85% of the local S wave velocity. We limit all test results to about 7 grids per shortest S wave wavelength (GPW). Each of the above simulations was

carried out with sufficient length to record not only the direct reflections for each seismic phase, but also reflections from opposing PML regions and corners. Other relevant source parameters are listed in Table 3.

[13] We now examine the performance of PML as implemented in the 3-D velocity-stress staggered-grid scheme. Simulations in homogeneous models for a variety of sources are examined first, followed by simulations in the presence of increasingly complex velocity structures, including extended rupture and 3-D structure tests.

3.2. PML Versus Reference (Homogeneous Case)

[14] The first set of tests take place in simulation space H1 and velocity structure M1. Figure 4 shows source S2 (Hector Mines strike-slip mechanism) as recorded at array site 2 with a PML region of thickness 10 (PML(10)). In each of the 3 components (X, Y, Z), no artificial reflections from the boundaries are observed, indicating that the PML regions provide sufficient absorption for both the nondispersive Rayleigh wave as well as the body wave phases. In Figure 5, source S1 (Northridge thrust mechanism) is recorded at array sites 1–8 and compared with reference traces. No artificial reflections are observed at any of the array sites. The reflection-free reference traces were produced by simulating the same event in a large model space with Dirichlet boundaries placed at a large distance from the source. This reference model space is capable of producing 25s of

reflection-free traces and is 749 nodes in the X and Y directions and 349 nodes deep. For this particular source, we also examine the PML performance for variable-width absorbing regions (5, 10, and 20). Figure 6 shows the difference, with respect to the reference traces, for each of the three widths. We choose to illustrate the error for all three components of motion, for which the error is expected to be similar. The error traces in the top plot (X component) have been magnified 100 times, indicating that the PML(5) regions typically absorb all but 1% of the outgoing energy. Error traces in the middle plot (Y component) have been magnified 250 times, showing that the PML(10) region allows maximum reflections of about 0.4% with respect to the maximums of the main seismic phases. Similarly, the Z component error traces for PML(20) (bottom plot) at 625 times magnification shows reduction of the outgoing amplitudes to below 0.16%. In the above homogeneous simulations, the absorption performance of both P and S waves as well as the nondispersive Rayleigh wave is tested. When comparing the relative amplitudes of various reflections in the error traces (e.g., Figure 6), we see that PML effectively damps all seismic phases present.

3.3. PML Versus Cerjan et al. (Homogeneous Case)

[15] The comparison to a reference model in the previous section revealed an impressive measure of absolute absorption by PML. Nevertheless, only superiority compared to other widely used absorbing boundary conditions with less than satisfactory performance should provide a reason to use PML in future applications. Therefore our second set of simulations compares the efficiency of various width PML regions to that of such a scheme, a standard Cerjan et al. absorbing boundary condition (width 20). The reasoning for choosing the Cerjan et al. scheme for comparison includes its apparent popularity, lack of instability problems (as opposed to many other efficient absorbers [see, e.g., *Ramahi*, 1999; *Imhof*, 2002; *Simone and Hestholm*, 1998; *Howell and Trefethen*, 1988]), and finally efficiency in connection with higher-order FD algorithms [*Hestholm et al.*, 1999]. Comparison with other popular absorbing boundary conditions or combinations thereof (for example, see *Wu and Fang* [1995] for comparison between and combination of PML and Higdons condition for EM) may provide additional insight, but is considered beyond the scope of our study.

[16] The first simulation in this series tests the absorption of broadband energy in the smaller model space (H2) using the homogeneous structure (M1). An explosive source (S4) recorded at array site 2 yields dramatic differences between the Cerjan et al.(20) and PML(10) schemes (Figure 7). Where the PML based scheme provides excellent absorption (no visibly reflected energy), the Cerjan et al. results are comparatively poor (Figure 7a). Examination of the amplitude spectra for the same traces indicates poor Cerjan et al. absorption across the simulation bandwidth, with the exception of the highest frequencies (Figure 7b). To determine how each scheme is performing as a function of frequency, we computed normalized residuals at each frequency $S_A(f)$ (Figure 7c)

$$S_A(f) = \frac{|R_A(f) - D_A(f)|}{R_A(f)}, \qquad (4)$$
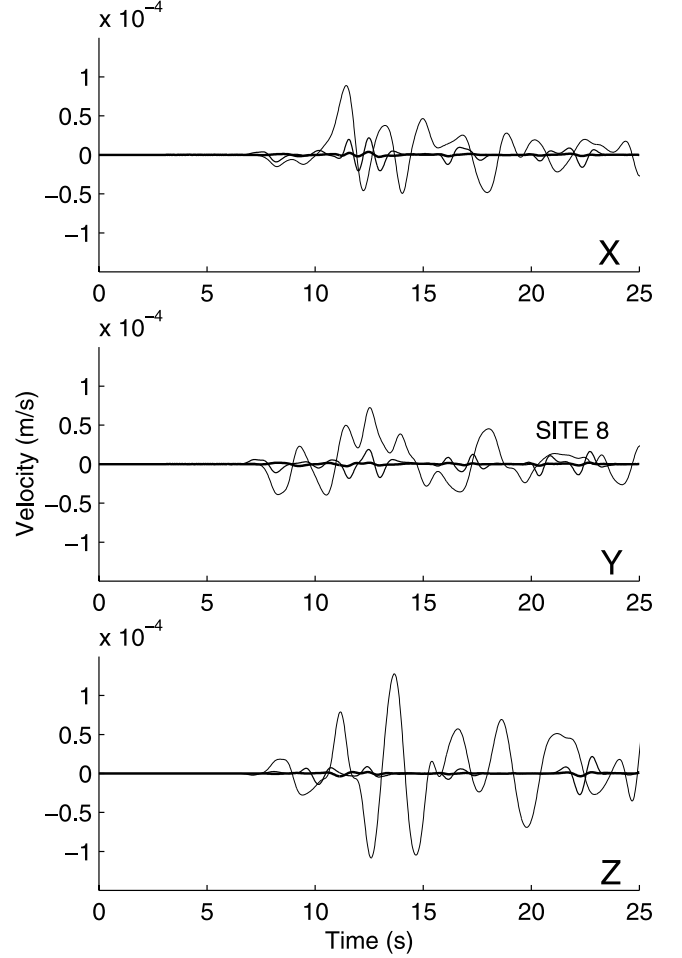
Figure 8. Error for PML and Cerjan et al. simulations recorded at array location 8 (see Figure 3). PML width 5 (medium solid) and 20 (thick solid) are compared to Cerjan et al. of width 20 (damping parameter 0.92, thin solid). Even the narrow PML region provides superior absorption over Cerjan et al. by a factor of 3 or more. Source is S1 and structure is M1, in larger space H1.

where R_A is the reference amplitude spectra and D_A is the test amplitude spectra. The normalized residuals suggest that on average PML (magnified 50 times relative to Cerjan et al.) provides consistent absorption across the simulation bandwidth. Figure 8 gives comparative error results, with respect to reference traces, for a larger model space (H1), structure (M1) and source (S1). The error records are given at site 8 for PML(5), PML(20) and Cerjan et al.(20). In this case, PML(5) provides superior results to Cerjan et al. by a factor of 3 or more. Finally, Figure 9 shows snapshots of PML and Cerjan et al. (widths 20) before (Figure 9a) and after (Figure 9b) the main seismic phases (P wave and S/Rayleigh waves) have left the simulation space. The Cerjan et al. scheme shows strong reflections from the boundaries, whereas PML results in no visible reflections. The model space, structure and source in this simulation were H1, M1 and S4, respectively.

3.4. One-Dimensional Tests

[17] We next examine the performance of PML(10) in a 1-D velocity structure, for which reference traces are also
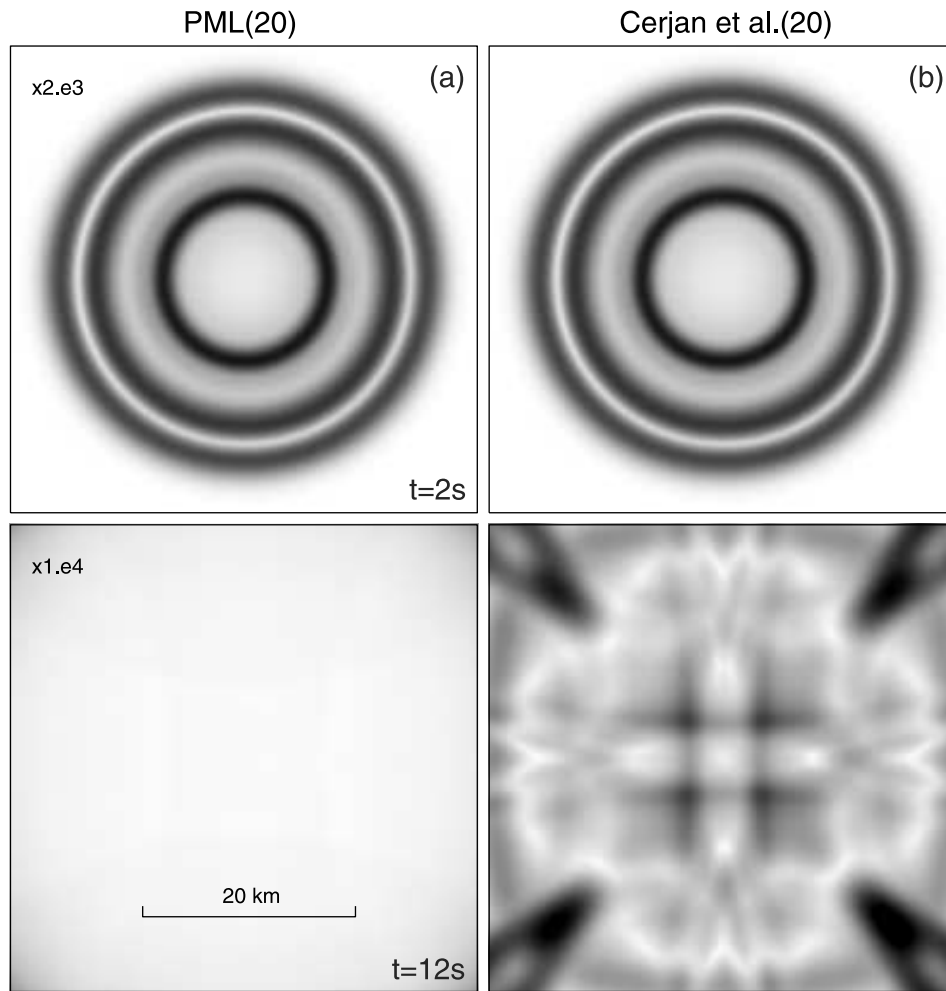
Figure 9. Explosive source (S4) wave field recorded on the free surface (model H1, structure M1) at 2 and 12 s. Snapshot set (a) is for PML(20) and snapshot set (b) is for Cerjan et al. (width 20). Snapshots at 2 s are amplified by a factor of 2 and snapshots at 12 s are amplified by 40. Note the large artificial reflections in the Cerjan et al. results. Snapshots depict the L_2 norm of the three velocity components.

computed. As mentioned previously, the 1-D profile through the LA basin and crust should serve as a sufficiently difficult (and realistic) test (V_s clamped to 1200 m/s, maximum V_p = 6185 m/s) using the single PML damping profile. In Figure 10 we show results for source S2 recorded at site 1 (X, Y and Z components) in model H3 and structure M2. As in the homogeneous case, no artificial reflections are observed at the viewing scale. Note that the performance of PML in the 1-D structure results, in addition to the direct phases, is challenged by dispersive surface waves (Rayleigh and Love) starting to emerge around 15 s in the records. Figure 11 shows the 1-D simulation results at all array sites, along with the reference traces and corresponding error (magnified 50 times). In this particular simulation space, typical reduction factors are about 1/200; although, a few low amplitude traces show reduced absorption. In general, the 1-D results are somewhat degraded as compared to the homogeneous tests. This is expected, as the single PML damping profile can only be constructed for an average or typical media velocity, even though a wide range of velocities are present in the

structure. In the Discussion section, we describe a possible method to improve PML's performance in the presence of heterogeneous media.

[18] Also in a 1-D structure (M3), results are presented for an extended rupture simulation (simulation space H4, Figure 12). Results for PML(10) and Cerjan et al.(20) are given at three sites adjacent to the fault. In addition, reference traces are superimposed at sites 1 and 2. These reference traces contain 50s (site 1) and 43s (site 2) of reflection-free traces computed in a model with dimensions 865 (X) by 800 (Y) by 442 (Z). Figure 12 shows excellent agreement between PML and reference traces while the Cerjan et al. results differ by up to a factor of two, both during the main rupture pulse and later arrivals. Notice also the permanent offset artifact of the velocity traces caused by the Cerjan et al. condition, which is not observed using PML; examination of the amplitude spectra reveals large differences between Cerjan et al. and the reference at low frequencies (<0.5 Hz). These results suggest that PML is able to significantly improve ground motion estimates for extended rupture
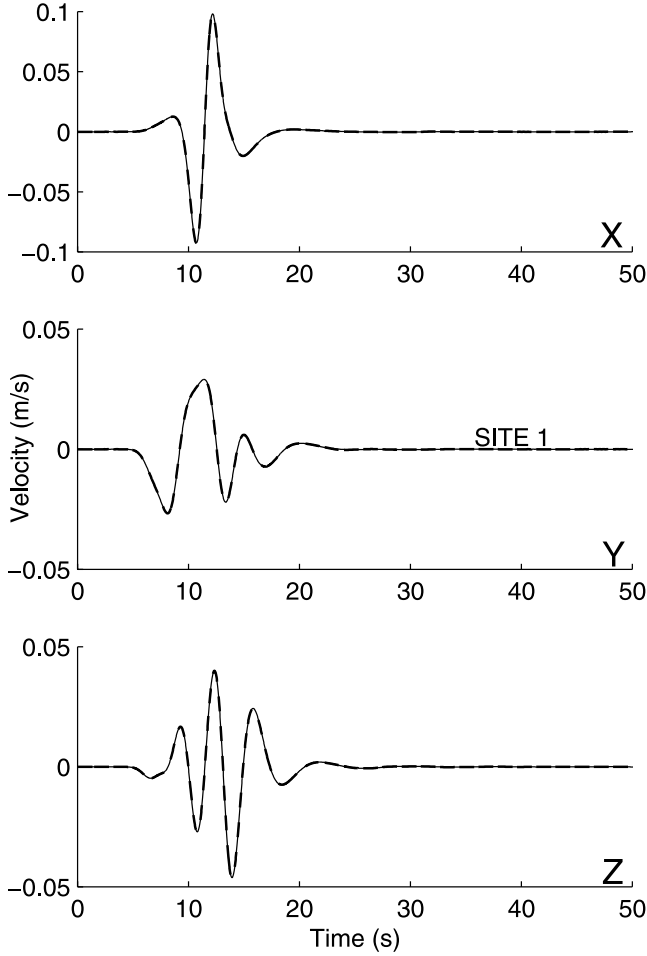
Figure 10. Source S2 (Hector Mines focal mechanism) recorded at array location 1 (see Figure 3) in the 1-D LA basin profile structure (M2) and model H3. PML width 10 (thick dash) is compared to reference traces (solid). No artificial reflections are observed at the viewing scale.

simulations, as compared to other layered absorbing boundary conditions.

3.5. Three-Dimensional Test

[19] Considering the widespread use of FD schemes for wave propagation in heterogeneous media, the final simulation results we present are for PML in a 3-D velocity structure (SCEC). As discussed previously, the 3-D structure simulation makes use of source S3 in structure M4 and in simulation space H5. Unfortunately, construction of reference traces for the complex structure case, i.e., for 3-D structure that extends to the simulation boundaries, is difficult. Thus, in this case, we simply compare results with that of Cerjan et al. A surface plan view of the clamped (1400 m/s) 3-D S wave velocity structure is shown in Figure 13, and PML(10) and Cerjan et al. (width 20) results are shown in Figure 14. At site 8 (northwest corner) boundary artifacts give rise to significant differences between the PML and Cerjan et al. waveforms, most notably that the primary phases on the latter are visibly influenced by spurious energy. At site 3, the primary differences between the waveforms are the result of trailing reflections in the

Cerjan et al. traces. Similar differences are observed at the remaining array sites.

3.6. Efficiency

[20] The PML condition requires little additional computational time, when compared to other layered schemes, e.g., Cerjan et al. However, due to the additional parallel and perpendicular components in the PML absorbing regions, PML is less efficient in terms of core memory. Although not representative of the most efficient storage scheme, an approximate multiplicative factor (f_{PML}) can be computed to estimate the memory required of a scheme with PML as
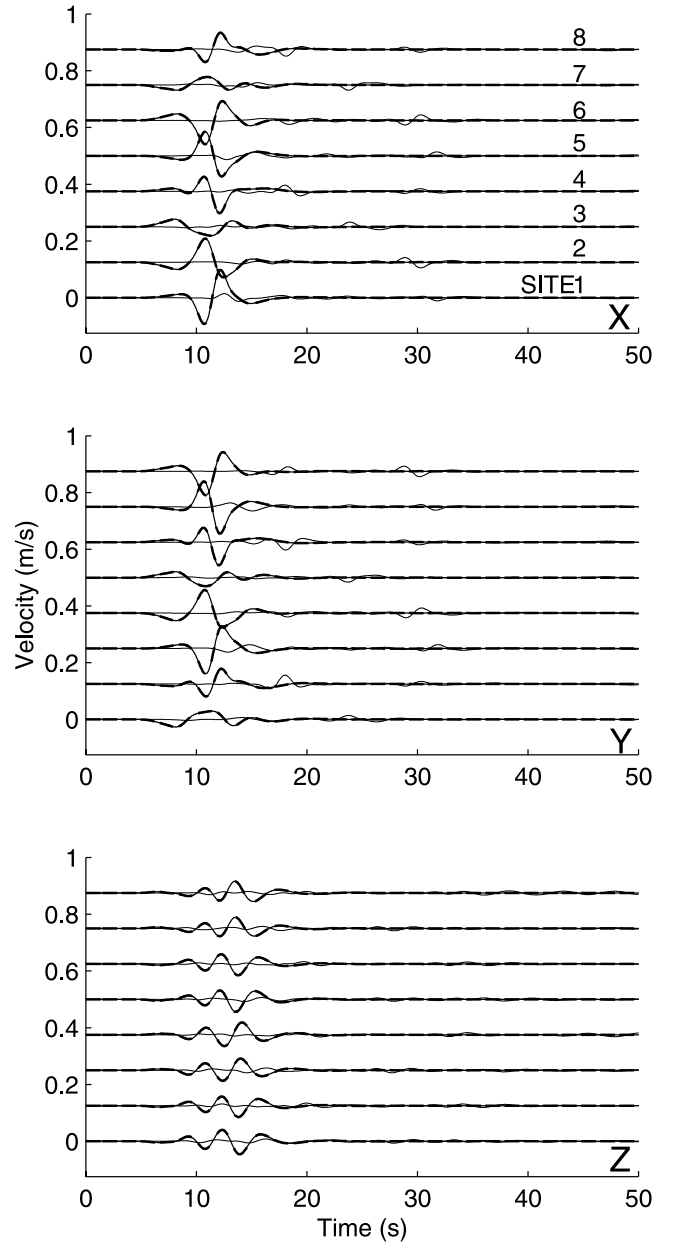
Figure 11. Simulation in Figure 10 shown for all array locations (see Figure 3). PML width 10 (thick dash) is compared to reference traces (medium solid). PML error (thin solid) is shown with corresponding traces and is amplified 50 times.
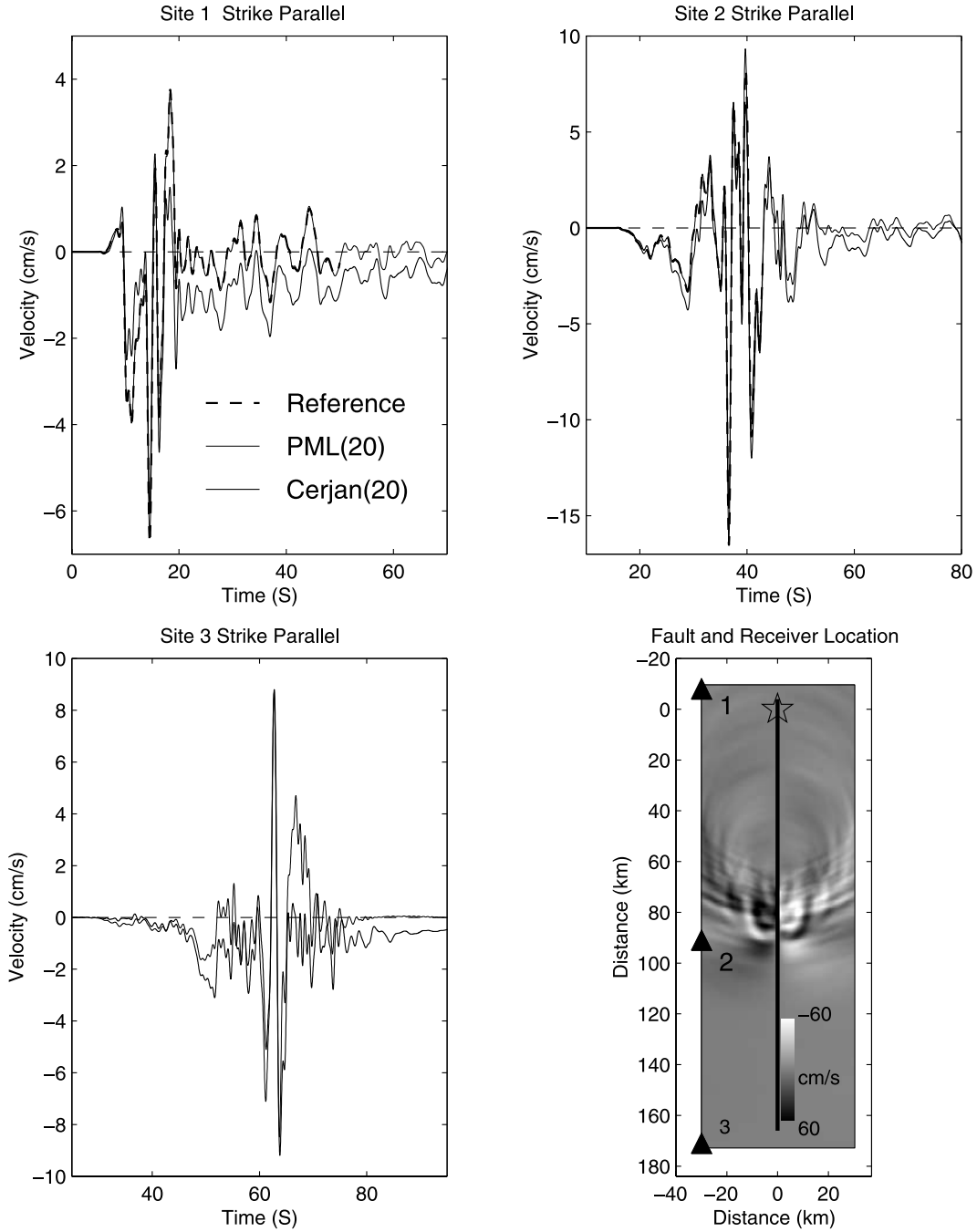
Figure 12. 1-Hz PML(10), Cerjan et al.(20) and reference traces for the extended rupture simulation and snapshot of rupture for the strike-parallel velocity. The reference traces are only computed to 50 s (site 1) and 43 s (site 2) due to computational limitations. On the snapshot, the line depicts the surface fault trace, the triangles indicate the location of recording sites 1–3, and the star shows the epicenter. Structure is M3 and simulation space is H4. Notice the excellent performance by PML, while Cerjan et al. generates factor-of-two amplitude error and permanent offset artifacts.

compared to a scheme which does not require additional storage in the absorbing region (e.g., Cerjan et al.)

$$f_{PML} = 1 + 3n_b\left(\frac{1}{n_x} + \frac{1}{n_y} + \frac{1}{2n_z}\right), \quad (5)$$

where n_x, n_y and n_z represent the number of total nodes in the three coordinate directions in the model space, and n_b

indicates the number of nodes near the boundaries reserved for the PML regions. The above equation assumes the presence of a free surface. A simple calculation shows that as the nodal dimensions increase for fixed width PML regions, the PML conditions account for a smaller percentage of the required total memory. However, due to the superb performance of PML, only thin PML regions are required to effectively suppress artificial reflections. As shown in
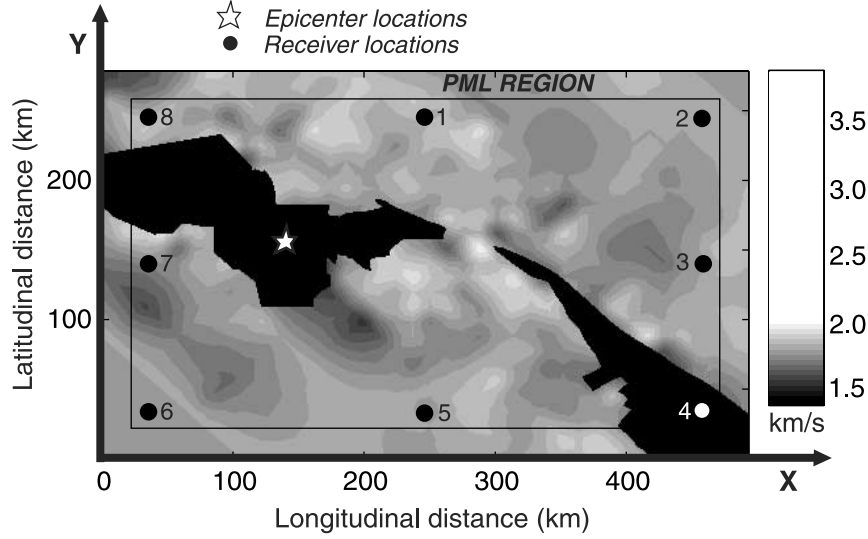
Figure 13. Clamped 3-D SCEC S wave velocity structure shown at the surface, containing a minimum shear velocity of 1400 m/s and supporting a maximum frequency of 0.2 Hz.

Table 4 for one of our particular model spaces, the use of PML results in decreased memory and increased efficiency for PML thicknesses less than 10 and 20, respectively, as compared to the Cerjan et al. or other similar schemes.

4. Stability

[21] In order for PML to become widely used in elasto-dynamic simulations the implementation must be stable for a wide range of models. It should be noted that some absorbing boundary conditions have been found to be unstable with schemes to solve both the electromagnetic (EM) [*Ramahi*, 1999] and elastodynamic [*Simone and Hestholm*, 1998; *Imhof*, 2002; *Higdon*, 1986, 1990] equations. Instabilities have also been found for PML applied to EM [*Nehrbass et al.*, 1996] and acoustic [*Hu*, 2001; *Tam et al.*, 1998] equations. *Teixeira et al.* [2001] and *Abarbanel and Gottlieb* [1997] showed mathematically that some PML methods are not strongly well-posed, and that small perturbations in the system can generate instability.

[22] We tested a number of different homogeneous, 1-D and 3-D velocity structures for stability using our PML implementation, and found problems only in certain 3-D media. No stability problems were encountered in any homogeneous or 1-D velocity structures, including 1-D velocity structures with large contrasts between layers. Randomized 1-D media also presented no problem. We only encountered a problem with instability in certain 3-D cases where structure with rapidly changing, large velocity contrasts (gradient magnitude as large as 15) was present in the PML region itself. In most cases, media smoothing within the PML prior to propagation was sufficient to restore stability.

Table 4. PML Efficiency

Absorbing Scheme (width)	Cerjan et al. (20)	PML (5)	PML (10)	PML (20)
Memory (normalized)	1.00	0.79	1.03	1.63
CPU-time (normalized)	1.00	0.41	0.58	1.04

[23] We mention two such smoothing approaches below, which may be used together or separately. The first technique involves extending the 3-D structure at the PML interface into the PML region; that is, the media value adjacent to the interface and within the interior region, is extended perpendicularly toward the boundary edge. We can represent such a strategy, for extension of parameter ξ in the Z direction, as

$$\xi_{i,j,k} = \xi_{i,j,k_o}, \tag{6}$$

where k_o is the value adjacent to the interface and where k indexes from the interface to the boundary edge. The second strategy is an example of smoothing the PML media by a multinode averaging process. We adopted a simple 5-point operator for smoothing in the plane PML regions. Such an operator, for parameter ξ in the Z plane, can be represented as

$$\xi_{i,j,k} = \frac{1}{5}\left(\xi_{i,j,k} + \xi_{i+1,j,k} + \xi_{i-1,j,k} + \xi_{i,j+1,k} + \xi_{i,j-1,k}\right) \tag{7}$$

and could be used in conjunction with the media extension operator. The effect of such an approach is to generate a locally quasi-homogeneous structure at a particular PML region location. No significant overhead in computational resources is required for either of the two smoothing methods.

5. Discussion

[24] The numerical results presented in this study make use of fourth-order operators in the interior region and second-order operators in the PML region. In the region near the PML interface, the operators are allowed to overlap. From the fourth-order interior region, operators sample one to two nodes deep in the PML region, depending on the wave field variable and location. Similarly, the second-order PML operators sample one node deep into the interior region. The mixing of operators at the PML interface
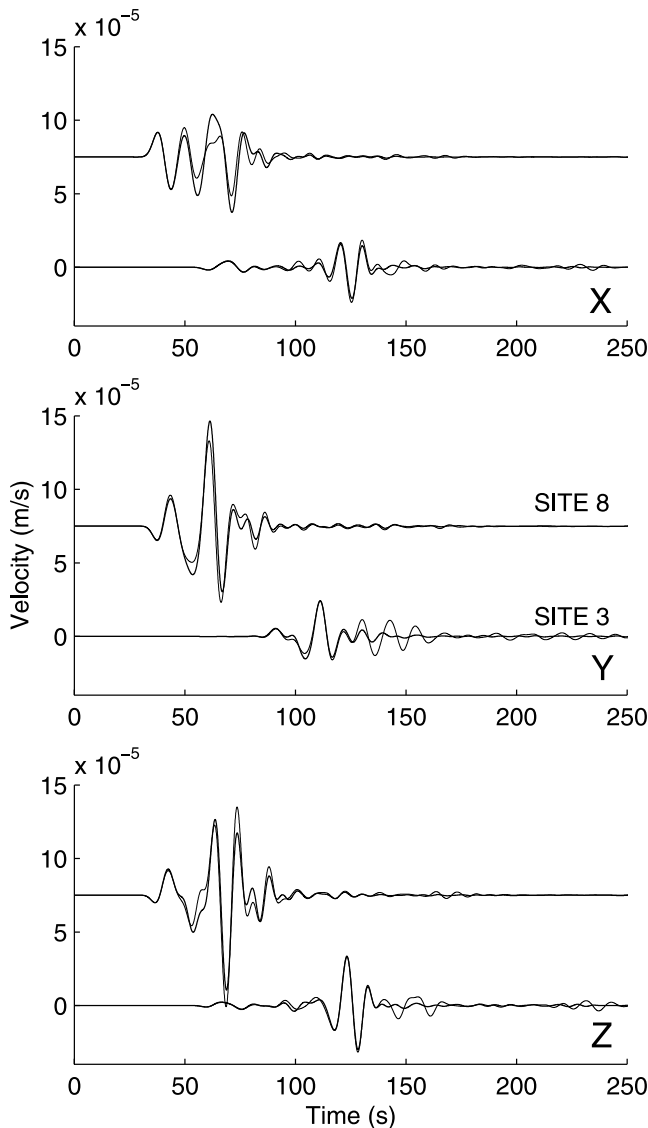
Figure 14. PML width 10 (thick) versus Cerjan et al. width 20 (thin) in a subspace of the SCEC 3-D reference structure. Cerjan et al. traces appear to be adversely affected by artificial reflections during (site 8) and after (site 3) the arrival of the primary phases. See Figure 13 for site locations.

apparently presents no difficulties; however, it is possible that improved accuracy may be obtained using fourth-order operators in the PML regions as well. *Chew and Liu* [1996] indicate that the PML error is proportional to the product of the discretization size and the damping contrast. Furthermore, it has been shown that this error (artificial reflections from the PML region) is due to the dispersion of the finite difference scheme [*Collino and Tsogka*, 2001]. Since higher-order operators, e.g., fourth-order, have the effect of mitigating numerical dispersion, we expect the application of fourth-order operators in the PML region to generate increased absorption, beyond that presented here. We conducted a cursory test of this property in a PML(10) simulation; that is, we compared the absorption results for simulations in which the grid spacing differed by a factor of 2 in each coordinate direction. In the scheme with reduced grid spacing, the PML region (width 10) is necessarily half the actual thickness of the original scheme; however, the absorption results were similar in both simulations. This result can likely be attributed to the reduction in numerical dispersion error in the reduced grid-spacing scheme. To implement the higher-order PML scheme, two areas need to be addressed: the free surface for certain PML regions and the outermost planes of the model space (PML regions). In the case of the free surface, use of the anti-symmetry relations to solve for velocity values above the grid is required [e.g., *Gottschämmer and Olsen*, 2001]. With regard to the latter concern, in the case of the fourth-order scheme, a typical approach is to invoke second-order operators on one to two nodes nearest the boundary. However, we believe that the performance of the second-order PML operators is sufficient for most current applications and we leave the development of higher-order operators for future work, if needed.

[25] Finally, we discuss the selection of V_s in equation (1) in arbitrary models. The current method for computing the maximum damping parameter (and subsequent damping value distribution) requires a representative value for V_s. This is straightforward in the homogeneous case; however, in media with 1-D and 3-D variations, the selection of a best value is less obvious. We found that taking the harmonic average of the minimum and maximum V_s values provided an optimal result in our 1-D simulation. Selection of a representative V_s in the 3-D case is more difficult, especially in the case of more extreme 3-D structures. One possible method is to initialize a suite of maximum damping values (damping distributions), which are based on the range of velocities present at the PML interface. This would allow the use of media-appropriate damping distributions, which may improve the performance of the PML even more.

[26] We have clearly demonstrated in our analysis that PML provides good amplitude reduction on both body and surface waves. Therefore in principle, the source may be located arbitrarily close to the PML and still generate the desired amplitude reduction. However, we have detected some numerical noise in synthetic seismograms recorded within a few grid points from the closest PML, for source locations similarly close to the absorbing boundary condition. We therefore recommend further tests if both the source and receivers are to be located less than 5 grid points from the closest PML boundary.

6. Conclusions

[27] We have implemented and tested the PML absorbing boundary condition in a 3-D fourth-order velocity-stress finite difference scheme, which includes a free-surface. Simulation results show PML's efficacy in the presence of all seismic phases for both explosive and double-couple sources. PML thickness 5, 10 and 20 typically reduce amplitudes to 1%, 0.4%, and 0.16%, respectively, of the maximum trace amplitude, leaving no observable reflections compared to the primary phases. Comparisons with a Cerjan et al. scheme suggest that PML is much more effective in reducing spurious reflections both during and after the arrival of the primary seismic phases. For exam-

ple, a PML thickness 5 region reduces amplitudes more than 3 times compared to a Cerjan et al. thickness 20 region in a half-space. In particular, PML tends to absorb relatively uniformly across the simulation bandwidth, including the long periods where the Cerjan et al. boundary condition seems to be less efficient. We show that synthetic seismograms with PML are in excellent agreement with reference traces at selected sites along an extended fault rupture. In contrast, the amplitude on the synthetics computed using Cerjan et al. absorbing boundary conditions are off by up to a factor of two, both during the main rupture pulse and for later arrivals. Moreover, permanent offset artifacts are generated by the Cerjan et al. conditions due to particularly poor performance at low frequencies. Finally, for a realistic 3-D structure the performance of PML is superior to that by Cerjan et al. in reducing the amplitude of spurious reflections during and after the direct arriving phases. The required computation time for PML is comparable to that of other layered schemes for a specific thickness, while PML is less efficient in terms of core memory due to additional components. However, both computational and storage requirements are significantly reduced for PML due to the superior performance for narrow regions. Stability problems were only encountered for 3-D models with very large velocity gradients, and smoothing of the structure within the PML was generally efficient in stabilizing the wave propagation.

Appendix A: Three-Dimensional Velocity-Stress and PML Systems

A1. Velocity-Stress System

[28] The 3-D isotropic, elastic velocity-stress system of equations is given as

$$\frac{\partial v_x}{\partial t} = \frac{1}{\rho}\left(\frac{\partial \sigma_{xx}}{\partial x} + \frac{\partial \sigma_{xy}}{\partial y} + \frac{\partial \sigma_{xz}}{\partial z}\right)$$

$$\frac{\partial v_y}{\partial t} = \frac{1}{\rho}\left(\frac{\partial \sigma_{xy}}{\partial x} + \frac{\partial \sigma_{yy}}{\partial y} + \frac{\partial \sigma_{yz}}{\partial z}\right)$$

$$\frac{\partial v_z}{\partial t} = \frac{1}{\rho}\left(\frac{\partial \sigma_{xz}}{\partial x} + \frac{\partial \sigma_{yz}}{\partial y} + \frac{\partial \sigma_{zz}}{\partial z}\right)$$

$$\frac{\partial \sigma_{xx}}{\partial t} = (\lambda + 2\mu)\frac{\partial v_x}{\partial x} + \lambda\left(\frac{\partial v_y}{\partial y} + \frac{\partial v_z}{\partial z}\right)$$

$$\frac{\partial \sigma_{yy}}{\partial t} = \lambda\frac{\partial v_x}{\partial x} + (\lambda + 2\mu)\frac{\partial v_y}{\partial y} + \lambda\frac{\partial v_z}{\partial z}$$

$$\frac{\partial \sigma_{zz}}{\partial t} = \lambda\left(\frac{\partial v_x}{\partial x} + \frac{\partial v_y}{\partial y}\right) + (\lambda + 2\mu)\frac{\partial v_z}{\partial z}$$

$$\frac{\partial \sigma_{xy}}{\partial t} = \mu\left(\frac{\partial v_x}{\partial y} + \frac{\partial v_y}{\partial x}\right)$$

$$\frac{\partial \sigma_{xz}}{\partial t} = \mu\left(\frac{\partial v_x}{\partial z} + \frac{\partial v_z}{\partial x}\right)$$

$$\frac{\partial \sigma_{yz}}{\partial t} = \mu\left(\frac{\partial v_y}{\partial z} + \frac{\partial v_z}{\partial y}\right),$$

where $\mathbf{v}(\mathbf{x}, t)$ is the velocity vector field, a function of both position $\mathbf{x}$ and time t, $\sigma(\mathbf{x}, t)$ is the stress tensor, $\lambda(\mathbf{x})$ and $\mu(\mathbf{x})$ are Lamé's elastic constants, and ρ is density.

A2. PML Formulations

[29] Modification of the velocity-stress system via the time domain equation-splitting procedure, for absorption in the X direction, results in the following PML system

$$\frac{\partial v_x^{\perp^x}}{\partial t} + d(x)v_x^{\perp^x} = \frac{1}{\rho}\frac{\partial \sigma_{xx}}{\partial x} \qquad \frac{\partial v_x^{\|^x}}{\partial t} = \frac{1}{\rho}\left(\frac{\partial \sigma_{xy}}{\partial y} + \frac{\partial \sigma_{xz}}{\partial z}\right)$$

$$\frac{\partial v_y^{\perp^x}}{\partial t} + d(x)v_y^{\perp^x} = \frac{1}{\rho}\frac{\partial \sigma_{xy}}{\partial x} \qquad \frac{\partial v_y^{\|^x}}{\partial t} = \frac{1}{\rho}\left(\frac{\partial \sigma_{yy}}{\partial y} + \frac{\partial \sigma_{yz}}{\partial z}\right)$$

$$\frac{\partial v_z^{\perp^x}}{\partial t} + d(x)v_z^{\perp^x} = \frac{1}{\rho}\frac{\partial \sigma_{xz}}{\partial x} \qquad \frac{\partial v_z^{\|^x}}{\partial t} = \frac{1}{\rho}\left(\frac{\partial \sigma_{yz}}{\partial y} + \frac{\partial \sigma_{zz}}{\partial z}\right)$$

$$\frac{\partial \sigma_{xx}^{\perp^x}}{\partial t} + d(x)\sigma_{xx}^{\perp^x} = (\lambda + 2\mu)\frac{\partial v_x}{\partial x} \qquad \frac{\partial \sigma_{xx}^{\|^x}}{\partial t} = \lambda\left(\frac{\partial v_y}{\partial y} + \frac{\partial v_z}{\partial z}\right)$$

$$\frac{\partial \sigma_{yy}^{\perp^x}}{\partial t} + d(x)\sigma_{yy}^{\perp^x} = \lambda\frac{\partial v_x}{\partial x} \qquad \frac{\partial \sigma_{yy}^{\|^x}}{\partial t} = (\lambda + 2\mu)\frac{\partial v_y}{\partial y} + \lambda\frac{\partial v_z}{\partial z}$$

$$\frac{\partial \sigma_{zz}^{\perp^x}}{\partial t} + d(x)\sigma_{zz}^{\perp^x} = \lambda\frac{\partial v_x}{\partial x} \qquad \frac{\partial \sigma_{zz}^{\|^x}}{\partial t} = \lambda\frac{\partial v_y}{\partial y} + (\lambda + 2\mu)\frac{\partial v_z}{\partial z}$$

$$\frac{\partial \sigma_{xy}^{\perp^x}}{\partial t} + d(x)\sigma_{xy}^{\perp^x} = \mu\frac{\partial v_y}{\partial x} \qquad \frac{\partial \sigma_{xy}^{\|^x}}{\partial t} = \mu\frac{\partial v_x}{\partial y}$$

$$\frac{\partial \sigma_{xz}^{\perp^x}}{\partial t} + d(x)\sigma_{xz}^{\perp^x} = \mu\frac{\partial v_z}{\partial x} \qquad \frac{\partial \sigma_{xz}^{\|^x}}{\partial t} = \mu\frac{\partial v_x}{\partial z}$$

$$\frac{\partial \sigma_{yz}^{\perp^x}}{\partial t} + d(x)\sigma_{yz}^{\perp^x} = 0 \qquad \frac{\partial \sigma_{yz}^{\|^x}}{\partial t} = \mu\left(\frac{\partial v_y}{\partial z} + \frac{\partial v_z}{\partial y}\right),$$

where $\perp^x$ indicates the component perpendicular to X, and $\|^x$ indicates the component(s) parallel to X [*Collino and Tsogka*, 2001]. Similar systems can be formed for absorption in the Y direction

$$\frac{\partial v_x^{\perp^y}}{\partial t} + d(y)v_x^{\perp^y} = \frac{1}{\rho}\frac{\partial \sigma_{xy}}{\partial y} \qquad \frac{\partial v_x^{\|^y}}{\partial t} = \frac{1}{\rho}\left(\frac{\partial \sigma_{xx}}{\partial x} + \frac{\partial \sigma_{xz}}{\partial z}\right)$$

$$\frac{\partial v_y^{\perp^y}}{\partial t} + d(y)v_y^{\perp^y} = \frac{1}{\rho}\frac{\partial \sigma_{yy}}{\partial y} \qquad \frac{\partial v_y^{\|^y}}{\partial t} = \frac{1}{\rho}\left(\frac{\partial \sigma_{xy}}{\partial x} + \frac{\partial \sigma_{yz}}{\partial z}\right)$$

$$\frac{\partial v_z^{\perp^y}}{\partial t} + d(y)v_z^{\perp^y} = \frac{1}{\rho}\frac{\partial \sigma_{yz}}{\partial y} \qquad \frac{\partial v_z^{\|^y}}{\partial t} = \frac{1}{\rho}\left(\frac{\partial \sigma_{xz}}{\partial x} + \frac{\partial \sigma_{zz}}{\partial z}\right)$$

$$\frac{\partial \sigma_{xx}^{\perp^y}}{\partial t} + d(y)\sigma_{xx}^{\perp^y} = \lambda\frac{\partial v_y}{\partial y} \qquad \frac{\partial \sigma_{xx}^{\|^y}}{\partial t} = (\lambda + 2\mu)\frac{\partial v_x}{\partial x} + \lambda\frac{\partial v_z}{\partial z}$$

$$\frac{\partial \sigma_{yy}^{\perp^y}}{\partial t} + d(y)\sigma_{yy}^{\perp^y} = (\lambda + 2\mu)\frac{\partial v_y}{\partial y} \qquad \frac{\partial \sigma_{yy}^{\|^y}}{\partial t} = \lambda\left(\frac{\partial v_x}{\partial x} + \frac{\partial v_z}{\partial z}\right)$$

$$\frac{\partial \sigma_{zz}^{\perp^y}}{\partial t} + d(y)\sigma_{zz}^{\perp^y} = \lambda\frac{\partial v_y}{\partial y} \qquad \frac{\partial \sigma_{zz}^{\|^y}}{\partial t} = \lambda\frac{\partial v_x}{\partial x} + (\lambda + 2\mu)\frac{\partial v_z}{\partial z}$$

$$\frac{\partial \sigma_{xy}^{\perp^y}}{\partial t} + d(y)\sigma_{xy}^{\perp^y} = \mu\frac{\partial v_x}{\partial y} \qquad \frac{\partial \sigma_{xy}^{\|^y}}{\partial t} = \mu\frac{\partial v_y}{\partial x}$$

$$\frac{\partial \sigma_{xz}^{\perp^y}}{\partial t} + d(y)\sigma_{xz}^{\perp^y} = 0 \qquad \frac{\partial \sigma_{xz}^{\|^y}}{\partial t} = \mu\left(\frac{\partial v_x}{\partial z} + \frac{\partial v_z}{\partial x}\right)$$

$$\frac{\partial \sigma_{yz}^{\perp^y}}{\partial t} + d(y)\sigma_{yz}^{\perp^y} = \mu\frac{\partial v_z}{\partial y} \qquad \frac{\partial \sigma_{yz}^{\|^y}}{\partial t} = \mu\frac{\partial v_y}{\partial z}$$

and for absorption in the Z direction

$$\frac{\partial v_x^{\perp z}}{\partial t} + d(z)v_x^{\perp z} = \frac{1}{\rho}\frac{\partial \sigma_{xz}}{\partial z} \qquad \frac{\partial v_x^{\parallel z}}{\partial t} = \frac{1}{\rho}\left(\frac{\partial \sigma_{xx}}{\partial x} + \frac{\partial \sigma_{xy}}{\partial y}\right)$$

$$\frac{\partial v_y^{\perp z}}{\partial t} + d(z)v_y^{\perp z} = \frac{1}{\rho}\frac{\partial \sigma_{yz}}{\partial z} \qquad \frac{\partial v_y^{\parallel z}}{\partial t} = \frac{1}{\rho}\left(\frac{\partial \sigma_{xy}}{\partial x} + \frac{\partial \sigma_{yy}}{\partial y}\right)$$

$$\frac{\partial v_z^{\perp z}}{\partial t} + d(z)v_z^{\perp z} = \frac{1}{\rho}\frac{\partial \sigma_{zz}}{\partial z} \qquad \frac{\partial v_z^{\parallel z}}{\partial t} = \frac{1}{\rho}\left(\frac{\partial \sigma_{xz}}{\partial x} + \frac{\partial \sigma_{yz}}{\partial y}\right)$$

$$\frac{\partial \sigma_{xx}^{\perp z}}{\partial t} + d(z)\sigma_{xx}^{\perp z} = \lambda\frac{\partial v_z}{\partial z} \qquad \frac{\partial \sigma_{xx}^{\parallel z}}{\partial t} = (\lambda + 2\mu)\frac{\partial v_x}{\partial x} + \lambda\frac{\partial v_y}{\partial y}$$

$$\frac{\partial \sigma_{yy}^{\perp z}}{\partial t} + d(z)\sigma_{yy}^{\perp z} = \lambda\frac{\partial v_z}{\partial z} \qquad \frac{\partial \sigma_{yy}^{\parallel z}}{\partial t} = \lambda\frac{\partial v_x}{\partial x} + (\lambda + 2\mu)\frac{\partial v_y}{\partial y}$$

$$\frac{\partial \sigma_{zz}^{\perp z}}{\partial t} + d(z)\sigma_{zz}^{\perp z} = (\lambda + 2\mu)\frac{\partial v_z}{\partial z} \qquad \frac{\partial \sigma_{zz}^{\parallel z}}{\partial t} = \lambda\left(\frac{\partial v_x}{\partial x} + \frac{\partial v_y}{\partial y}\right)$$

$$\frac{\partial \sigma_{xy}^{\perp z}}{\partial t} + d(z)\sigma_{xy}^{\perp z} = 0 \qquad \frac{\partial \sigma_{xy}^{\parallel z}}{\partial t} = \mu\left(\frac{\partial v_x}{\partial y} + \frac{\partial v_y}{\partial x}\right)$$

$$\frac{\partial \sigma_{xz}^{\perp z}}{\partial t} + d(z)\sigma_{xz}^{\perp z} = \mu\frac{\partial v_x}{\partial z} \qquad \frac{\partial \sigma_{xz}^{\parallel z}}{\partial t} = \mu\frac{\partial v_z}{\partial x}$$

$$\frac{\partial \sigma_{yz}^{\perp z}}{\partial t} + d(z)\sigma_{yz}^{\perp z} = \mu\frac{\partial v_y}{\partial z} \qquad \frac{\partial \sigma_{yz}^{\parallel z}}{\partial t} = \mu\frac{\partial v_z}{\partial y}$$

A3.   Generalization and Second-Order Discretization

[30]   The above systems for absorption in the X, Y and Z directions can be generalized into a single system appropriate for damping on any single plane or combination of planes, i.e., edges and corners. Such a system for the 3-D velocity-stress scheme in its discretized form follows

$$(V_x)_{i,j,k}^{n+1} = \left(V_x^x\right)_{i,j,k}^{n+1} + \left(V_x^y\right)_{i,j,k}^{n+1} + \left(V_x^z\right)_{i,j,k}^{n+1}$$

$$\frac{\left(V_x^x\right)_{i,j,k}^{n+1} - \left(V_x^x\right)_{i,j,k}^{n}}{\Delta t} + d_i^x\frac{\left(V_x^x\right)_{i,j,k}^{n+1} + \left(V_x^x\right)_{i,j,k}^{n}}{2} = \frac{\left(\Sigma_{xx}\right)_{i+\frac{1}{2},j,k}^{n+\frac{1}{2}} - \left(\Sigma_{xx}\right)_{i-\frac{1}{2},j,k}^{n+\frac{1}{2}}}{\rho\Delta x}$$

$$\frac{\left(V_x^y\right)_{i,j,k}^{n+1} - \left(V_x^y\right)_{i,j,k}^{n}}{\Delta t} + d_j^y\frac{\left(V_x^y\right)_{i,j,k}^{n+1} + \left(V_x^y\right)_{i,j,k}^{n}}{2} = \frac{\left(\Sigma_{xy}\right)_{i,j+\frac{1}{2},k}^{n+\frac{1}{2}} - \left(\Sigma_{xy}\right)_{i,j-\frac{1}{2},k}^{n+\frac{1}{2}}}{\rho\Delta y}$$

$$\frac{\left(V_x^z\right)_{i,j,k}^{n+1} - \left(V_x^z\right)_{i,j,k}^{n}}{\Delta t} + d_k^z\frac{\left(V_x^z\right)_{i,j,k}^{n+1} + \left(V_x^z\right)_{i,j,k}^{n}}{2} = \frac{\left(\Sigma_{xz}\right)_{i,j,k+\frac{1}{2}}^{n+\frac{1}{2}} - \left(\Sigma_{xz}\right)_{i,j,k-\frac{1}{2}}^{n+\frac{1}{2}}}{\rho\Delta z}$$

$$(V_y)_{i+\frac{1}{2},j+\frac{1}{2},k}^{n+1} = \left(V_y^x\right)_{i+\frac{1}{2},j+\frac{1}{2},k}^{n+1} + \left(V_y^y\right)_{i+\frac{1}{2},j+\frac{1}{2},k}^{n+1} + \left(V_y^z\right)_{i+\frac{1}{2},j+\frac{1}{2},k}^{n+1}$$

$$\frac{\left(V_y^x\right)_{i+\frac{1}{2},j+\frac{1}{2},k}^{n+1} - \left(V_y^x\right)_{i+\frac{1}{2},j+\frac{1}{2},k}^{n}}{\Delta t} + d_{i+1/2}^x\frac{\left(V_y^x\right)_{i+\frac{1}{2},j+\frac{1}{2},k}^{n+1} + \left(V_y^x\right)_{i+\frac{1}{2},j+\frac{1}{2},k}^{n}}{2}$$

$$= \frac{\left(\Sigma_{xy}\right)_{i+1,j+\frac{1}{2},k}^{n+\frac{1}{2}} - \left(\Sigma_{xy}\right)_{i,j+\frac{1}{2},k}^{n+\frac{1}{2}}}{\rho\Delta x}$$

$$\frac{\left(V_y^y\right)_{i+\frac{1}{2},j+\frac{1}{2},k}^{n+1} - \left(V_y^y\right)_{i+\frac{1}{2},j+\frac{1}{2},k}^{n}}{\Delta t} + d_{j+1/2}^y\frac{\left(V_y^y\right)_{i+\frac{1}{2},j+\frac{1}{2},k}^{n+1} + \left(V_y^y\right)_{i+\frac{1}{2},j+\frac{1}{2},k}^{n}}{2}$$

$$= \frac{\left(\Sigma_{yy}\right)_{i+\frac{1}{2},j+1,k}^{n+\frac{1}{2}} - \left(\Sigma_{yy}\right)_{i+\frac{1}{2},j,k}^{n+\frac{1}{2}}}{\rho\Delta y}$$

$$\frac{\left(V_y^z\right)_{i+\frac{1}{2},j+\frac{1}{2},k}^{n+1} - \left(V_y^z\right)_{i+\frac{1}{2},j+\frac{1}{2},k}^{n}}{\Delta t} + d_k^z\frac{\left(V_y^z\right)_{i+\frac{1}{2},j+\frac{1}{2},k}^{n+1} + \left(V_y^z\right)_{i+\frac{1}{2},j+\frac{1}{2},k}^{n}}{2}$$

$$= \frac{\left(\Sigma_{yz}\right)_{i+\frac{1}{2},j+\frac{1}{2},k+\frac{1}{2}}^{n+\frac{1}{2}} - \left(\Sigma_{yz}\right)_{i+\frac{1}{2},j+\frac{1}{2},k-\frac{1}{2}}^{n+\frac{1}{2}}}{\rho\Delta z}$$

$$(V_z)_{i+\frac{1}{2},j,k+\frac{1}{2}}^{n+1} = \left(V_z^x\right)_{i+\frac{1}{2},j,k+\frac{1}{2}}^{n+1} + \left(V_z^y\right)_{i+\frac{1}{2},j,k+\frac{1}{2}}^{n+1} + \left(V_z^z\right)_{i+\frac{1}{2},j,k+\frac{1}{2}}^{n+1}$$

$$\frac{\left(V_z^x\right)_{i+\frac{1}{2},j,k+\frac{1}{2}}^{n+1} - \left(V_z^x\right)_{i+\frac{1}{2},j,k+\frac{1}{2}}^{n}}{\Delta t} + d_{i+1/2}^x\frac{\left(V_z^x\right)_{i+\frac{1}{2},j,k+\frac{1}{2}}^{n+1} + \left(V_z^x\right)_{i+\frac{1}{2},j,k+\frac{1}{2}}^{n}}{2}$$

$$= \frac{\left(\Sigma_{xz}\right)_{i+1,j,k+\frac{1}{2}}^{n+\frac{1}{2}} - \left(\Sigma_{xz}\right)_{i,j,k+\frac{1}{2}}^{n+\frac{1}{2}}}{\rho\Delta x}$$

$$\frac{\left(V_z^y\right)_{i+\frac{1}{2},j,k+\frac{1}{2}}^{n+1} - \left(V_z^y\right)_{i+\frac{1}{2},j,k+\frac{1}{2}}^{n}}{\Delta t} + d_j^y\frac{\left(V_z^y\right)_{i+\frac{1}{2},j,k+\frac{1}{2}}^{n+1} + \left(V_z^y\right)_{i+\frac{1}{2},j,k+\frac{1}{2}}^{n}}{2}$$

$$= \frac{\left(\Sigma_{yz}\right)_{i+\frac{1}{2},j+\frac{1}{2},k+\frac{1}{2}}^{n+\frac{1}{2}} - \left(\Sigma_{yz}\right)_{i+\frac{1}{2},j-\frac{1}{2},k+\frac{1}{2}}^{n+\frac{1}{2}}}{\rho\Delta y}$$

$$\frac{\left(V_z^z\right)_{i+\frac{1}{2},j,k+\frac{1}{2}}^{n+1} - \left(V_z^z\right)_{i+\frac{1}{2},j,k+\frac{1}{2}}^{n}}{\Delta t} + d_{k+1/2}^z\frac{\left(V_z^z\right)_{i+\frac{1}{2},j,k+\frac{1}{2}}^{n+1} + \left(V_z^z\right)_{i+\frac{1}{2},j,k+\frac{1}{2}}^{n}}{2}$$

$$= \frac{\left(\Sigma_{zz}\right)_{i+\frac{1}{2},j,k+1}^{n+\frac{1}{2}} - \left(\Sigma_{zz}\right)_{i+\frac{1}{2},j,k}^{n+\frac{1}{2}}}{\rho\Delta z}$$

$$(\Sigma_{xx})_{i+\frac{1}{2},j,k}^{n+\frac{1}{2}} = \left(\Sigma_{xx}^x\right)_{i+\frac{1}{2},j,k}^{n+\frac{1}{2}} + \left(\Sigma_{xx}^y\right)_{i+\frac{1}{2},j,k}^{n+\frac{1}{2}} + \left(\Sigma_{xx}^z\right)_{i+\frac{1}{2},j,k}^{n+\frac{1}{2}}$$

$$\frac{\left(\Sigma_{xx}^x\right)_{i+\frac{1}{2},j,k}^{n+\frac{1}{2}} - \left(\Sigma_{xx}^x\right)_{i+\frac{1}{2},j,k}^{n-\frac{1}{2}}}{\Delta t} + d_{i+1/2}^x\frac{\left(\Sigma_{xx}^x\right)_{i+\frac{1}{2},j,k}^{n+\frac{1}{2}} + \left(\Sigma_{xx}^x\right)_{i+\frac{1}{2},j,k}^{n-\frac{1}{2}}}{2}$$

$$= (\lambda + 2\mu)\frac{(V_x)_{i+1,j,k}^{n} - (V_x)_{i,j,k}^{n}}{\Delta x}$$

$$\frac{\left(\Sigma_{xx}^y\right)_{i+\frac{1}{2},j,k}^{n+\frac{1}{2}} - \left(\Sigma_{xx}^y\right)_{i+\frac{1}{2},j,k}^{n-\frac{1}{2}}}{\Delta t} + d_j^y\frac{\left(\Sigma_{xx}^y\right)_{i+\frac{1}{2},j,k}^{n+\frac{1}{2}} + \left(\Sigma_{xx}^y\right)_{i+\frac{1}{2},j,k}^{n-\frac{1}{2}}}{2}$$

$$= \lambda\frac{(V_y)_{i+\frac{1}{2},j+\frac{1}{2},k}^{n} - (V_y)_{i+\frac{1}{2},j-\frac{1}{2},k}^{n}}{\Delta y}$$

$$\frac{\left(\Sigma_{xx}^z\right)_{i+\frac{1}{2},j,k}^{n+\frac{1}{2}} - \left(\Sigma_{xx}^z\right)_{i+\frac{1}{2},j,k}^{n-\frac{1}{2}}}{\Delta t} + d_k^z\frac{\left(\Sigma_{xx}^z\right)_{i+\frac{1}{2},j,k}^{n+\frac{1}{2}} + \left(\Sigma_{xx}^z\right)_{i+\frac{1}{2},j,k}^{n-\frac{1}{2}}}{2}$$

$$= \lambda\frac{(V_z)_{i+\frac{1}{2},j,k+\frac{1}{2}}^{n} - (V_z)_{i+\frac{1}{2},j,k-\frac{1}{2}}^{n}}{\Delta z}$$

$$(\Sigma_{yy})_{i+\frac{1}{2},j,k}^{n+\frac{1}{2}} = \left(\Sigma_{yy}^x\right)_{i+\frac{1}{2},j,k}^{n+\frac{1}{2}} + \left(\Sigma_{yy}^y\right)_{i+\frac{1}{2},j,k}^{n+\frac{1}{2}} + \left(\Sigma_{yy}^z\right)_{i+\frac{1}{2},j,k}^{n+\frac{1}{2}}$$

$$\frac{\left(\Sigma_{yy}^x\right)_{i+\frac{1}{2},j,k}^{n+\frac{1}{2}} - \left(\Sigma_{yy}^x\right)_{i+\frac{1}{2},j,k}^{n-\frac{1}{2}}}{\Delta t} + d_{i+1/2}^x\frac{\left(\Sigma_{yy}^x\right)_{i+\frac{1}{2},j,k}^{n+\frac{1}{2}} + \left(\Sigma_{yy}^x\right)_{i+\frac{1}{2},j,k}^{n-\frac{1}{2}}}{2}$$

$$= \lambda\frac{(V_x)_{i+1,j,k}^{n} - (V_x)_{i,j,k}^{n}}{\Delta x}$$

$$\frac{\left(\Sigma_{yy}^y\right)_{i+\frac{1}{2},j,k}^{n+\frac{1}{2}} - \left(\Sigma_{yy}^y\right)_{i+\frac{1}{2},j,k}^{n-\frac{1}{2}}}{\Delta t} + d_j^y\frac{\left(\Sigma_{yy}^y\right)_{i+\frac{1}{2},j,k}^{n+\frac{1}{2}} + \left(\Sigma_{yy}^y\right)_{i+\frac{1}{2},j,k}^{n-\frac{1}{2}}}{2}$$

$$= (\lambda + 2\mu)\frac{(V_y)_{i+\frac{1}{2},j+\frac{1}{2},k}^{n} - (V_y)_{i+\frac{1}{2},j-\frac{1}{2},k}^{n}}{\Delta y}$$

$$\frac{\left(\Sigma_{yy}^z\right)_{i+\frac{1}{2},j,k}^{n+\frac{1}{2}} - \left(\Sigma_{yy}^z\right)_{i+\frac{1}{2},j,k}^{n-\frac{1}{2}}}{\Delta t} + d_k^z\frac{\left(\Sigma_{yy}^z\right)_{i+\frac{1}{2},j,k}^{n+\frac{1}{2}} + \left(\Sigma_{yy}^z\right)_{i+\frac{1}{2},j,k}^{n-\frac{1}{2}}}{2}$$

$$= \lambda\frac{(V_z)_{i+\frac{1}{2},j,k+\frac{1}{2}}^{n} - (V_z)_{i+\frac{1}{2},j,k-\frac{1}{2}}^{n}}{\Delta z}$$

$$\left(\Sigma_{zz}\right)^{n+\frac{1}{2}}_{i+\frac{1}{2},j,k} = \left(\Sigma^x_{zz}\right)^{n+\frac{1}{2}}_{i+\frac{1}{2},j,k} + \left(\Sigma^y_{zz}\right)^{n+\frac{1}{2}}_{i+\frac{1}{2},j,k} + \left(\Sigma^z_{zz}\right)^{n+\frac{1}{2}}_{i+\frac{1}{2},j,k}$$

$$\frac{\left(\Sigma^x_{zz}\right)^{n+\frac{1}{2}}_{i+\frac{1}{2},j,k} - \left(\Sigma^x_{zz}\right)^{n-\frac{1}{2}}_{i+\frac{1}{2},j,k}}{\Delta t} + d^x_{i+1/2}\frac{\left(\Sigma^x_{zz}\right)^{n+\frac{1}{2}}_{i+\frac{1}{2},j,k} + \left(\Sigma^x_{zz}\right)^{n-\frac{1}{2}}_{i+\frac{1}{2},j,k}}{2}$$

$$= \lambda\frac{(V_x)^n_{i+1,j,k} - (V_x)^n_{i,j,k}}{\Delta x}$$

$$\frac{\left(\Sigma^y_{zz}\right)^{n+\frac{1}{2}}_{i+\frac{1}{2},j,k} - \left(\Sigma^y_{zz}\right)^{n-\frac{1}{2}}_{i+\frac{1}{2},j,k}}{\Delta t} + d^y_j\frac{\left(\Sigma^y_{zz}\right)^{n+\frac{1}{2}}_{i+\frac{1}{2},j,k} + \left(\Sigma^y_{zz}\right)^{n-\frac{1}{2}}_{i+\frac{1}{2},j,k}}{2}$$

$$= \lambda\frac{(V_y)^n_{i+\frac{1}{2},j+\frac{1}{2},k} - (V_y)^n_{i+\frac{1}{2},j-\frac{1}{2},k}}{\Delta y}$$

$$\frac{\left(\Sigma^z_{zz}\right)^{n+\frac{1}{2}}_{i+\frac{1}{2},j,k} - \left(\Sigma^z_{zz}\right)^{n-\frac{1}{2}}_{i+\frac{1}{2},j,k}}{\Delta t} + d^z_k\frac{\left(\Sigma^z_{zz}\right)^{n+\frac{1}{2}}_{i+\frac{1}{2},j,k} + \left(\Sigma^z_{zz}\right)^{n-\frac{1}{2}}_{i+\frac{1}{2},j,k}}{2}$$

$$= (\lambda + 2\mu)\frac{(V_z)^n_{i+\frac{1}{2},j,k+\frac{1}{2}} - (V_z)^n_{i+\frac{1}{2},j,k-\frac{1}{2}}}{\Delta z}$$

$$\left(\Sigma_{xy}\right)^{n+\frac{1}{2}}_{i,j+\frac{1}{2},k} = \left(\Sigma^x_{xy}\right)^{n+\frac{1}{2}}_{i,j+\frac{1}{2},k} + \left(\Sigma^y_{xy}\right)^{n+\frac{1}{2}}_{i,j+\frac{1}{2},k} + \left(\Sigma^z_{xy}\right)^{n+\frac{1}{2}}_{i,j+\frac{1}{2},k}$$

$$\frac{\left(\Sigma^x_{xy}\right)^{n+\frac{1}{2}}_{i,j+\frac{1}{2},k} - \left(\Sigma^x_{xy}\right)^{n-\frac{1}{2}}_{i,j+\frac{1}{2},k}}{\Delta t} + d^x_i\frac{\left(\Sigma^x_{xy}\right)^{n+\frac{1}{2}}_{i,j+\frac{1}{2},k} + \left(\Sigma^x_{xy}\right)^{n-\frac{1}{2}}_{i,j+\frac{1}{2},k}}{2}$$

$$= \mu\frac{(V_y)^n_{i+\frac{1}{2},j+\frac{1}{2},k} - (V_y)^n_{i-\frac{1}{2},j+\frac{1}{2},k}}{\Delta x}$$

$$\frac{\left(\Sigma^y_{xy}\right)^{n+\frac{1}{2}}_{i,j+\frac{1}{2},k} - \left(\Sigma^y_{xy}\right)^{n-\frac{1}{2}}_{i,j+\frac{1}{2},k}}{\Delta t} + d^y_{j+1/2}\frac{\left(\Sigma^y_{xy}\right)^{n+\frac{1}{2}}_{i,j+\frac{1}{2},k} + \left(\Sigma^y_{xy}\right)^{n-\frac{1}{2}}_{i,j+\frac{1}{2},k}}{2}$$

$$= \mu\frac{(V_x)^n_{i,j+1,k} - (V_x)^n_{i,j,k}}{\Delta y}$$

$$\frac{\left(\Sigma^z_{xy}\right)^{n+\frac{1}{2}}_{i,j+\frac{1}{2},k} - \left(\Sigma^z_{xy}\right)^{n-\frac{1}{2}}_{i,j+\frac{1}{2},k}}{\Delta t} + d^z_k\frac{\left(\Sigma^z_{xy}\right)^{n+\frac{1}{2}}_{i,j+\frac{1}{2},k} + \left(\Sigma^z_{xy}\right)^{n-\frac{1}{2}}_{i,j+\frac{1}{2},k}}{2} = 0$$

$$\left(\Sigma_{xz}\right)^{n+\frac{1}{2}}_{i,j,k+\frac{1}{2}} = \left(\Sigma^x_{xz}\right)^{n+\frac{1}{2}}_{i,j,k+\frac{1}{2}} + \left(\Sigma^y_{xz}\right)^{n+\frac{1}{2}}_{i,j,k+\frac{1}{2}} + \left(\Sigma^z_{xz}\right)^{n+\frac{1}{2}}_{i,j,k+\frac{1}{2}}$$

$$\frac{\left(\Sigma^x_{xz}\right)^{n+\frac{1}{2}}_{i,j,k+\frac{1}{2}} - \left(\Sigma^x_{xz}\right)^{n-\frac{1}{2}}_{i,j,k+\frac{1}{2}}}{\Delta t} + d^x_i\frac{\left(\Sigma^x_{xz}\right)^{n+\frac{1}{2}}_{i,j,k+\frac{1}{2}} + \left(\Sigma^x_{xz}\right)^{n-\frac{1}{2}}_{i,j,k+\frac{1}{2}}}{2}$$

$$= \mu\frac{(V_z)^n_{i+\frac{1}{2},j,k+\frac{1}{2}} - (V_z)^n_{i-\frac{1}{2},j,k+\frac{1}{2}}}{\Delta x}$$

$$\frac{\left(\Sigma^y_{xz}\right)^{n+\frac{1}{2}}_{i,j,k+\frac{1}{2}} - \left(\Sigma^y_{xz}\right)^{n-\frac{1}{2}}_{i,j,k+\frac{1}{2}}}{\Delta t} + d^y_j\frac{\left(\Sigma^y_{xz}\right)^{n+\frac{1}{2}}_{i,j,k+\frac{1}{2}} + \left(\Sigma^y_{xz}\right)^{n-\frac{1}{2}}_{i,j,k+\frac{1}{2}}}{2} = 0$$

$$\frac{\left(\Sigma^z_{xz}\right)^{n+\frac{1}{2}}_{i,j,k+\frac{1}{2}} - \left(\Sigma^z_{xz}\right)^{n-\frac{1}{2}}_{i,j,k+\frac{1}{2}}}{\Delta t} + d^z_{k+1/2}\frac{\left(\Sigma^z_{xz}\right)^{n+\frac{1}{2}}_{i,j,k+\frac{1}{2}} + \left(\Sigma^z_{xz}\right)^{n-\frac{1}{2}}_{i,j,k+\frac{1}{2}}}{2}$$

$$= \mu\frac{(V_x)^n_{i,j,k+1} - (V_x)^n_{i,j,k}}{\Delta z}$$

$$\left(\Sigma_{yz}\right)^{n+\frac{1}{2}}_{i+\frac{1}{2},j+\frac{1}{2},k+\frac{1}{2}} = \left(\Sigma^x_{yz}\right)^{n+\frac{1}{2}}_{i+\frac{1}{2},j+\frac{1}{2},k+\frac{1}{2}} + \left(\Sigma^y_{yz}\right)^{n+\frac{1}{2}}_{i+\frac{1}{2},j+\frac{1}{2},k+\frac{1}{2}} + \left(\Sigma^z_{yz}\right)^{n+\frac{1}{2}}_{i+\frac{1}{2},j+\frac{1}{2},k+\frac{1}{2}}$$

$$\frac{\left(\Sigma^x_{yz}\right)^{n+\frac{1}{2}}_{i+\frac{1}{2},j+\frac{1}{2},k+\frac{1}{2}} - \left(\Sigma^x_{yz}\right)^{n-\frac{1}{2}}_{i+\frac{1}{2},j+\frac{1}{2},k+\frac{1}{2}}}{\Delta t}$$

$$+ d^x_{i+1/2}\frac{\left(\Sigma^x_{yz}\right)^{n+\frac{1}{2}}_{i+\frac{1}{2},j+\frac{1}{2},k+\frac{1}{2}} + \left(\Sigma^x_{yz}\right)^{n-\frac{1}{2}}_{i+\frac{1}{2},j+\frac{1}{2},k+\frac{1}{2}}}{2} = 0$$

$$\frac{\left(\Sigma^y_{yz}\right)^{n+\frac{1}{2}}_{i+\frac{1}{2},j+\frac{1}{2},k+\frac{1}{2}} - \left(\Sigma^y_{yz}\right)^{n-\frac{1}{2}}_{i+\frac{1}{2},j+\frac{1}{2},k+\frac{1}{2}}}{\Delta t} + d^y_{j+1/2}$$

$$\cdot\frac{\left(\Sigma^y_{yz}\right)^{n+\frac{1}{2}}_{i+\frac{1}{2},j+\frac{1}{2},k+\frac{1}{2}} + \left(\Sigma^y_{yz}\right)^{n-\frac{1}{2}}_{i+\frac{1}{2},j+\frac{1}{2},k+\frac{1}{2}}}{2}$$

$$= \mu\frac{(V_z)^n_{i+\frac{1}{2},j+1,k+\frac{1}{2}} - (V_z)^n_{i+\frac{1}{2},j,k+\frac{1}{2}}}{\Delta y}$$

$$\frac{\left(\Sigma^z_{yz}\right)^{n+\frac{1}{2}}_{i+\frac{1}{2},j+\frac{1}{2},k+\frac{1}{2}} - \left(\Sigma^z_{yz}\right)^{n-\frac{1}{2}}_{i+\frac{1}{2},j+\frac{1}{2},k+\frac{1}{2}}}{\Delta t} + d^z_{k+1/2}$$

$$\cdot\frac{\left(\Sigma^z_{yz}\right)^{n+\frac{1}{2}}_{i+\frac{1}{2},j+\frac{1}{2},k+\frac{1}{2}} + \left(\Sigma^z_{yz}\right)^{n-\frac{1}{2}}_{i+\frac{1}{2},j+\frac{1}{2},k+\frac{1}{2}}}{2}$$

$$= \mu\frac{(V_y)^n_{i+\frac{1}{2},j+\frac{1}{2},k+1} - (V_y)^n_{i+\frac{1}{2},j+\frac{1}{2},k}}{\Delta z}$$

References

Abarbanel, S., and D. Gottlieb, A mathematical analysis of the PML method, *J. Comput. Phys.*, *134*, 357–363, 1997.

Berenger, J., A perfectly matched layer for the absorption of electromagnetic waves, *J. Comput. Geophys.*, *114*, 185–200, 1994.

Berenger, J., Three-dimensional perfectly matched layer for the absorption of electromagnetic waves, *J. Comput. Geophys.*, *127*, 363–379, 1996.

Cerjan, C., D. Kosloff, R. Kosloff, and M. Reshef, A non-reflecting boundary condition for direct acoustic and elastic wave equations, *Geophysics*, *50*, 705–708, 1985.

Chew, W., and Q. Liu, Perfectly matched layers for elastodynamics: A new absorbing boundary condition, *J. Comput. Acoust.*, *4*(4), 341–359, 1996.

Clayton, R., and B. Engquist, Absorbing boundary conditions for acoustic and elastic wave equations, *Bull. Seismol. Soc. Am.*, *67*, 1529–1540, 1977.

Collino, F., and C. Tsogka, Application of the perfectly matched absorbing layer model to the linear elastodynamic problem in anisotropic heterogeneous media, *Geophysics*, *66*(1), 294–307, 2001.

Gottschämmer, E., and K. B. Olsen, Accuracy of the explicit planar free-surface boundary condition implemented in a fourth-order staggered-grid velocity-stress finite-difference scheme, *Bull. Seismol. Soc. Am.*, *91*, 617–623, 2001.

Graves, R. W., Three-dimensional finite-difference modeling of the San Andreas fault: source parameterization and ground motion levels, *Bull. Seismol. Soc. Am.*, *88*, 881–897, 1998.

Hastings, F., J. Schneider, and S. Broschat, Application of the perfectly matched layer (PML) absorbing boundary condition to elastic wave propagation, *J. Acoust. Soc. Am.*, *100*(5), 3061–3069, 1996.

Hestholm, S. O., B. O. Ruud, and E. S. Husebye, 3-D versus 2-D finite-difference seismic synthetics including real surface topography, *Phys. Earth Planet. Inter.*, *113*, 339–354, 1999.

Higdon, R., Absorbing boundary conditions for difference approximations to the multidimensional wave equation, *Math. Comput.*, *47*, 437–459, 1986.

Higdon, R., Radiation boundary conditions for elastic wave propagation, *SIAM J. Numer. Anal.*, *27*, 831–870, 1990.

Howell, L. H., and L. N. Trefethen, Ill-posedness of absorbing boundary conditions for migration, *Geophysics*, *53*, 593–603, 1988.

Hu, F. Q., A stable, perfectly matched layer for linearized Euler equations in unsplit physical variables, *J. Comput. Phys.*, *173*, 455–480, 2001.

Imhof, M. G., A stable optimal absorbing boundary condition for acoustic finite-difference, *J. Seismic Exp.*, 10, 281–291, 2002.

Liu, Q., and J. Tao, The perfectly matched layer for acoustic waves in absorptive media, *J. Acoust. Soc. Am.*, 102(4), 2072–2082, 1997.

Madariaga, R., Dynamics of an expanding circular fault, *Bull. Seismol. Soc. Am.*, 66, 639–667, 1976.

Magistrale, H., S. Day, R. Clayton, and R. Graves, The SCEC southern California reference three-dimensional seismic velocity model version 2, *Bull. Seismol. Soc. Am.*, 90(6), S65–S76, 2000.

Nehrbass, J. W., J. F. Lee, and R. Lee, Stability analysis for perfectly matched layered absorbers, *Electromagnetics*, 16, 385–397, 1996.

Nielsen, S. B., and K. B. Olsen, Constraints on stress and friction from dynamic rupture models of the 1994 Northridge, California, earthquake, *Pure Appl. Geophys.*, 157, 2029–2046, 2000.

Olsen, K. B., Simulation of three-dimensional wave propagation in the Salt Lake Basin, Ph.D. thesis, 157 pp., Univ. of Utah, Salt Lake City, 1994.

Olsen, K. B., Site amplification in the Los Angeles basin from 3D modeling of ground motion, *Bull. Seismol. Soc. Am.*, 90, S77–S94, 2000.

Olsen, K. B., Three-dimensional ground motion simulations for large earthquakes on the San Andreas fault with dynamic and observational constraints, *J. Comput. Acoust.*, 9(3), 1203–1215, 2001.

Olsen, K. B., and R. J. Archuleta, Three-dimensional simulation of earthquakes on the Los Angeles fault system, *Bull. Seismol. Soc. Am.*, 86, 575–596, 1996.

Olsen, K. B., R. J. Archuleta, and J. R. Matarese, Three-dimensional simulation of a magnitude 7.75 earthquake on the San Andreas fault, *Science*, 270, 1628–1632, 1995.

Olsen, K. B., R. Madariaga, and R. J. Archuleta, Three-dimensional dynamic simulation of the 1992 Landers earthquake, *Science*, 278, 834–838, 1997.

Olsen, K. B., R. Nigbor, and T. Konno, 3D viscoelastic wave propagation in the Upper Borrego Valley, California, constrained by borehole and surface data, *Bull. Seismol. Soc. Am.*, 90, 134–150, 2000.

Peyrat, S., K. B. Olsen, and R. Madariaga, Dynamic modeling of the 1992 Landers earthquake, *J. Geophys. Res.*, 106, 26,467–26,482, 2001.

Ramahi, O. M., Stability of absorbing boundary conditions, *IEEE Trans. Antennas Propag.*, 47, 593–599, 1999.

Randall, C. J., Absorbing boundary condition for the elastic wave equation, *Geophysics*, 53, 611–624, 1988.

Reynolds, A. C., Boundary conditions for the numerical solution of wave propagation problems, *Geophysics*, 43, 1099–1110, 1978.

Simone, A., and S. Hestholm, Instabilities in applying absorbing boundary conditions to high-order seismic modeling algorithms, *Geophysics*, 63, 1017–1023, 1998.

Tam, C. K. W., L. Auriault, and F. Cambuli, Perfectly matched layer as an absorbing boundary condition for the linearized Euler equations in open and ducted domains, *J. Comput. Phys.*, 144, 213–234, 1998.

Teixeira, F. L., K. P. Hwang, W. C. Chew, and J. M. Jin, Conformal PML-FDTD schemes for electromagnetic field simulations: A dynamic stability study, *IEEE Trans. Antennas Propag.*, 49, 902–907, 2001.

Virieux, J., P-SV wave propagation in heterogeneous media: Velocity-stress finite-difference method, *Geophysics*, 51, 889–901, 1986.

Virieux, J., and R. Madariaga, Dynamic faulting studied by a finite-difference method, *Bull. Seismol. Soc. Am.*, 72, 345–369, 1982.

Wald, D., and R. W. Graves, The seismic response of the Los Angeles basin, California, *Bull. Seismol. Soc. Am.*, 88, 337–356, 1998.

Wald, D., and T. Heaton, Spatial and temporal distribution of slip for the 1992 Landers, California earthquake, *Bull. Seismol. Soc. Am.*, 84(3), 668–691, 1994.

Wu, Z. H., and J. Y. Fang, Numerical implementation and performance of perfectly matched layer boundary condition for wave guide structures, *IEEE Trans. Microwave Theory Techniques*, 43, 2676–2683, 1995.

Zeng, Y., and Q. Liu, Acoustic detection of buried objects in 3-D fluid saturated porous media: Numerical modelling, *IEEE Trans. Geosci. Remote Sens.*, 39, 1165–1173, 2001.

Zeng, Y., J. Q. He, and Q. H. Liu, The application of the perfectly matched layer in numerical modeling of wave propagation in poroelastic media, *Geophysics*, 66, 1258–1266, 2001.

—————————

C. Marcinkovich, ExxonMobil Exploration Company, 222 Benmar, Houston, TX 77060, USA.

K. Olsen, Institute for Crustal Studies, University of California, Santa Barbara, CA 93106, USA. (kbolsen@crustal.ucsb.edu)